Universidade de Aveiro
2021

Diana Sofia
Antunes Pereira

Sensores em fibra ótica baseados numa fibra de núcleo oco quadrado

Optical fiber sensors based on a hollow square core fiber

Universidade de Aveiro
2021

Diana Sofia Antunes Pereira

Sensores em fibra ótica baseados numa fibra de núcleo oco quadrado

Optical fiber sensors based on a hollow square core fiber

Dissertação apresentada à Universidade de Aveiro para cumprimento dos requisitos necessários à obtenção do grau de Mestre em Engenharia Física, realizada sob a orientação científica da Doutora Marta Sofia dos Anjos Ferreira, Investigadora Júnior do i3N e do Departamento de Física da Universidade de Aveiro.

o júri / the jury

presidente / president

Prof. Doutor Leonel Marques Vitorino Joaquim
Professor Auxiliar do Departamento de Física da Universidade de Aveiro

vogais / examiners committee

Doutora Marta Sofia dos Anjos Ferreira
Investigadora Júnior do Departamento de Física da Universidade de Aveiro (orientadora)

Prof. Doutor José Luís Campos de Oliveira Santos
Professor Catedrático da Faculdade de Ciências da Universidade do Porto

agradecimentos / acknowledgements

Queria agradecer em primeiro lugar à minha orientadora, Doutora Marta Sofia dos Anjos Ferreira, por toda a ajuda prestada ao longo deste trabalho, pela disponibilidade, paciência e por todos os conhecimentos transmitidos. Obrigada por sempre me incentivares e por me fazeres dar sempre o meu melhor, mas acima de tudo, obrigada por teres acreditado em mim ao longo deste trabalho.

Ao projeto AROMA, financiado pelo FEDER, através do CENTRO2020 - Programa Operacional Regional do Centro, CENTRO-01-0145-FEDER-031568, e pelos fundos nacionais (OE), PTDC/EEI-EEE/31568/2017, UIDB/50025/2020 & UIDP/50025/2020, através da FCT/MCTES. Também agradeço à cooperação bilateral FCT/DAAD (FLOW, Project ID: 57518590) por possibilitar a visita as laboratórios do Leibniz Institute of Photonic Technology (Leibniz-IPHT).

Ao Departamento de Física da Universidade de Aveiro, e ao I3N pelas condições oferecida e materiais cedidos que possibilitaram a realização deste trabalho.

Ao Leibniz-IPHT por facultar a fibra que foi utilizada mediante este trabalho, bem como aos colegas deste instituto pelo conhecimento transmitido.

Aos meus amigos e colegas pelo companheirismo e apoio prestado.

Aos meus pais por todo o apoio moral imprescindível e ajuda dados durante esta etapa.

E, por último, gostaria de agradecer ao meu irmão. Obrigada por tudo o que me transmitiste: positivismo, conhecimento, paciência, força e segurança. Obrigada por seres o pilar que me faz sempre querer alcançar mais e melhor.

Palavras Chave

Fibra de núcleo oco quadrado, sensores em fibra ótica, antirressonância, interferência de Mach-Zehnder, interferência multimodal.

Resumo

No presente trabalho pretendeu-se explorar o uso de uma fibra de núcleo oco antirressonante, como elementos sensores. Estes dispositivos foram desenvolvidos com uma configuração em transmissão, sendo a propagação efetuada através de duas antirressonâncias. Esta permitiu também o aparecimento de interferência multimodal e de Mach-Zehnder. Com o intuito de usar estas componentes interferométricas como elementos sensores, o dispositivo foi empregue tanto em meios líquidos, como no ar.

Posteriormente, foi elaborada uma caracterização ao sensor de fibra de núcleo oco quadrado em soluções aquosas de glucose. A resposta deste foi estudada a variações do índice de refração, e calibrada à região espetral da fonte ótica utilizada. Além disso, foi estudada a influência do comprimento do sensor, tendo-se observado que existe um comprimento para o qual a sensibilidade atingida é otimizada. Adicionalmente, foi elaborada uma caracterização ao índice de refração com compensação da temperatura.

Ainda no contexto da análise em meios líquidos, o sensor foi imergido em soluções aquosas de etanol, com o intuito de monitorizar o perfil de evaporação de compostos orgânicos voláteis. Efetuou-se uma monitorização da resposta espetral do sensor relativamente às soluções, o que permitiu obter, de forma satisfatória, uma variação em tempo real da concentração de etanol.

Finalmente, realizou-se uma caracterização do sensor a diferentes parâmetros físicos, tendo-se usado duas bandas espetrais distintas. Na primeira banda, $1530\,\mathrm{nm} - 1610\,\mathrm{nm}$, caracterizou-se a interferência de Mach-zehnder, a ressonância externa e a interferência multimodal a variações da temperatura, curvatura e tensão. Na segunda banda, $900\,\mathrm{nm} - 1300\,\mathrm{nm}$, caracterizou-se as ressonâncias externa e interna a variações da temperatura e curvatura. Em ambos os casos, a medição simultânea dos parâmetros em estudo foi também proposta.

O sensor desenvolvido revelou-se altamente promissor nas várias experiências realizadas, onde, em muitas situações, se destacou de outros sensores já reportados. Por ser um dispositivo que apresenta reduzidas dimensões, elevadas robustez, e capaz de medir simultaneamente a vários parâmetros, sem recorrer a configurações complexas, a sua implementação poderá vir ter impacto em diversas aplicações.

Keywords Hollow square core fiber, optical fiber sensors, antiresonance, Mach-Zehnder interference, Multimodal interference.

Abstract

In the current work, the development of optical fiber sensors based on an antiresonant hollow core fiber was aimed. The sensing structures were developed in a transmission configuration enhancing two antiresonance propagations, along with the multimode interference and Mach-Zehnder interference. With the objective of using these interferometric components as sensing elements, the sensor was employed in both liquid and air media.

Initially, a numerical analysis was addressed to both internal and external antiresonances. A simulation on the effective refractive index of the fundamental core mode was also carried out, achieving results that are in good agreement with both numerical and theoretical models. Furthemore, a comparison between the expected and experimental transmission spectra was established observing, in an overall view, similar modulations.

In a posterior stage, a characterization of the hollow square core fiber sensor was performed in glucose aqueous solutions. The sensor response was studied to variations in the refractive index, and calibrated to the wavelength range of the optical source utilized. Moreover, the influence of the sensor length was studied, observing the existance of an optimum length where the maximum sensitivity is enhanced. A temperature independent refractive index detection was also established.

Still in the framework of this theme, and with the objective of monitoring the evaporation profile of volatile organic compounds, the sensor was embedded in ethanol aqueous solutions. The monitoring of the sensor response towards the solutions was carried out, allowing to successfully attain a real time variation of the ethanol concentration.

Finally, the sensor was characterized to different physical parameters in an air environment, where two broadbands were used. In the first band, $1530\,\mathrm{nm}$ - $1610\,\mathrm{nm}$, a characterization to the temperature, curvature, and strain was performed for the Mach-Zehnder interference, external resonance, and multimode interference. In the second broadband, $900\,\mathrm{nm}$ - $1300\,\mathrm{nm}$, the external and internal resonances were characterize to both temperature and curvature. In both cases, the simultaneous measurement of the parameters under study was also proposed.

The studied inline sensor revealed to be highly promising in the several experiments that were conducted, where, in many cases, stood out from other sensors that were already reported in the literature. Its reduced dimensions, high robustness, and capability to simultaneously measure different parameters, and making a temperature discrimination, without needing a complex design configuration, makes it extremely viable in the implementation on several applications.

Contents

List of Figures

List of Symbols

C	Curvature
C_L	Confinement loss
D	Distance between the fixed stage and translation stage
d_h	Diameter of the air holes in MOFs
F	Air fraction in MOFs
h	Height of the bending
k_0	Vacuum wavenumber
k_{a}	Core wavenumber
$K_{C,\mathrm{ER}}$	ER sensitivity to curvature
$K_{C,\mathrm{IR}}$	IR sensitivity to curvature
$K_{C,\mathrm{MMI}}$	MMI sensitivity to curvature
$K_{C,\mathrm{MZI}}$	MZI sensitivity to curvature
$K_{\varepsilon,\mathrm{ER}}$	ER sensitivity to strain
$K_{\varepsilon,\mathrm{MMI}}$	MMI sensitivity to strain
$K_{\varepsilon,\mathrm{MZI}}$	MZI sensitivity to strain
$K_{T,\mathrm{ER}}$	ER sensitivity to temperature
$K_{T,\mathrm{IR}}$	IR sensitivity to temperature
$K_{T,\mathrm{MMI}}$	MMI sensitivity to temperature
$K_{T,\mathrm{MZI}}$	MZI sensitivity to temperature
L	Length of the HSCF
m	Resonance order
n_{a}	Refractive index of air
$n_{\mathrm{a}v}$	Average refractive index of the MOF's cladding
n_{eff}	Effective refractive index
$n_{\mathrm{eff}}^{\mathrm{a}}$	Effective refractive index of the air core
$n_{\mathrm{eff}}^{\mathrm{cl}_i}$	Effective refractive index of the cladding mode i
$n_{\mathrm{eff}}^{\mathrm{cl}_j}$	Effective refractive index of the cladding mode j
$n_{\mathrm{eff}}^{\mathrm{Si}}$	Effective refractive index of the silica strands
n_{comp}	Temperature compensated refractive index
n_{Si}	Refractive index of silica
p	Wavelength order interference
r	Core radius
R	Bending radius
w	Thickness of the FP resonator

α	Thermal expansion coefficient
β	Thermo-optic coefficient
δn	Minimum value of refractive index
ΔC	Variation of curvature
$\Delta\varepsilon$	Variation of strain
$\Delta\phi$	Phase shift
$\Delta\lambda$	Mean wavelength shift
$\Delta\lambda_{\mathrm{ER}}$	ER response (wavelength shift)
$\Delta\lambda_{\mathrm{IR}}$	IR response (wavelength shift)
$\Delta\lambda_{\mathrm{MMI}}$	MMI response (wavelength shift)
$\Delta\lambda_{\mathrm{MZI}}$	MZI response (wavelength shift)
Δn	Variation of refractive index between two solutions
Δn_{eff}	Difference of the effective refractive indices of silica and air
$\Delta n_{\mathrm{eff}}^{\mathrm{cl}}$	Difference of the effective refractive indices of cladding modes
Δr	Difference of the optical path
ΔT	Variation of temperature
ϵ	Square fraction of the refractive indices of silica and air
$\Im(n_{\mathrm{eff}})$	Imaginary part of the effective refractive index
$j_{m-1,n}$	n^{th} root of the Bessel function $m-1$
ϕ	Accumulated phase
Λ	Pitch of the air holes in MOFs
λ	Wavelength
λ_1	Wavelength of peak 1
λ_2	Wavelength of peak 2
λ_{comp}	Temperature compensated wavelength
λ_m	Resonance wavelength
λ_{MMI}	Interference wavelength of the MMI
λ_{MZI}	Interference wavelength of the MZI
$\Re(n_{\mathrm{eff}})$	Real part of the effective refractive index
ω	Mass fraction of solution
ρ_{11}	Component of the strain-optic tensor
ρ_{12}	Component of the strain-optic tensor
ρ_ε	Effective photoelastic coefficient of fused silica
ρ_ε^i	Photoelastic coefficient of silica the mode i experiences
ρ_ε^j	Photoelastic coefficient of silica the mode j experiences
σ	Perturbation parameter
σ_λ	Maximum wavelength standart deviation
θ	Incident angle
υ	Poisson ratio

Acronyms

AR	Antiresonance
ARHCF	Antiresonant hollow core fiber
ARROW	Antiresonant reflecting optical waveguide
ER	External resonance
FBG	Fiber Bragg grating
FFT	Fast Fourier transform
FPI	Fabry-Perot interference
FSR	Free spectral range
HC-PCF	Hollow core photonic crystal fiber
HSCF	Hollow square core fiber
IC	Inhibited coupling
IR	Internal resonance
LPG	Long period grating
MI	Michelson interference
MMI	Multimodal interference
MMF	Multimode fiber
MOF	Microstructured optical fiber
MTIR	Modified total internal reflection
MZI	Mach-Zehnder interference
OFS	Optical fiber sensor
PBG	Photonic bandgap
PCF	Photonic crystal fiber
SC-PCF	Solid core photonic crystal fiber
SI	Sagnac interference
SMF	Singlemode fiber
TEC	Thermal expansion coefficient
TIR	Total internal reflection
TOC	Thermo-optic coefficient
VOC	Volatile organic compound

1. Introduction

1.1 Overview

One of the greatest marks on the optical field started in the 20^{th} century with the development of the optical fiber. The concept that light could be guided within a restricted medium through the total internal reflection (TIR) effect was already developed in 1854, derived from the experiments conducted by Tyndall [1]. Knowing that light could propagate in a material, if the right conditions were met, triggered the scientists at the time on the major applications it could be employed, especially in the communication field. From that moment, several attempts were conducted to design a successful waveguide that could transmit light with some effectiveness. The optical glass fibers were the first fibers to be made [1]. However, due to the high losses that they presented and the technology still in development, those fibers could only be successfully implemented in medical applications [2]. In an attempt to widen the use of optical fibers in other fields, such as optical communications, where a low attenuation was required to transmit the data, the scientists started to explore new ways of achieving the desired characteristics. A successful low loss fiber was developed in 1966, by Charles Kao, who figured that the silica's higher purity would lead to a decrease in the attenuation [3, 4]. With this discovery and with the breakthrough of the laser, also in the '60s [4], a true mark began not only in the telecommunication area but also in the sensing field. These would suffer a huge burst over the following decades, though, in the context of this work, the focus will be on the sensing field.

The electronic sensors were developed before the optical fiber sensors (OFS) which led to an intensive usage on many different applications. However, due to the notorious advantages of the optical fiber sensors in many aspects, namely the immunity to electromagnetic interference, high reliability and small dimensions [4, 5], their prospects of use were highly noticed. They could be easily implemented in many adverse situations where the electronic sensors could not. With this, the scientific community focused on exploring this technology, enhancing the use of OFS as an alternative sensing technology suitable in many applications [6]. Over the years, a huge variety of sensors were developed, giving rise to a panoply of configurations with the most dissimilar functioning. Even so, one of the main interests, that was not achieved at the time, relied on attaining sensors that would respond over certain bandwidths/frequencies. This would be accomplished by designing new configurations of optical fibers that could easily manipulate some of the optical properties.

The photonic bandgap effect (PBG) started being studied by Yablonovitch in the late '80s [7]. It was known that certain materials which presented a periodicity, exhibited frequency bands, namely the photonic bandgap, where the propagation of electromagnetic waves

was prohibited [7]. This effect stirred up a huge interest, leading to studies on possible implementations of this concept on waveguides. The requirements needed to design a waveguide based on this effect, such as having a proper periodic structure, with dimensions in the wavelength scale [8], made it extremely difficult to achieve a practical implementation. Due to these constrains and the lack of means at the time, the development of a fiber based on this principle was strenuous to achieve. The pursuit on developing a fiber with the proper microstructures was only acomplished in 1996, with a successful creation of a solid central core fiber surrounded by air channels, that guided light throught a process akin to the TIR effect [9]. Only three years later, a fiber based on the PBG effect was utterly carried out [10]. With these achievements, merged a new class of fibers, namely the microstructured optical fiber (MOF), or photonic crystal fiber (PCF).

MOFs can present a solid core or a hollow core, feature that allows different light guidance mechanisms. Typically on MOFs that have a solid core, the light guidance occurs through the modified total internal reflection (MTIR) whereas in hollow core, the guidance mechanism relies on the PBG effect or by the inhibited coupling (IC) [3, 9]. This new category of waveguides, soon attracted the attention of the scientific community due to its unique capability on manipulating and controlling the optical properties of light, such as birefringence, dispersion, and nonlinearities [11]. This showed great promise not only in low loss communication but also in many sensing applications. With the advances in the photonic technology ground, the sensing field was significantly enhanced, craving the interest and urge to unveil new types of MOFs that could allow and flourish other intrinsic optical properties.

Currently, there is a variety of PCF designs with different physical mechanisms that can manipulate and modulate light, and that are employed to monitor several physical, chemical, and biological parameters. OFS typically work based on the principle of light interference or by resourting to fiber gratings, such as fiber Bragg gratings (FBG) or long period gratings (LPG), though, other mechanisms can also be used [12]. Among the interferometer-based sensors, those based on multimode interference (MMI), Mach-Zehnder interference (MZI), Fabry-Perot interference (FPI), Michelson interference (MI), and Sagnac interference (SI) should be highlighted. The multiple interferometric events carried out by the highly diversed PCF sensors allowed an improvement on the implementation of these on several applications over the past few years. On table 1.1 are indicated some PCF sensors based on interferometry, as well as some other OFS, recently designed to monitor physical parameters.

From a brief view of the described sensors, in table 1.1, one can see the continuous growth of PCFs in the sensing field over the years. Not only they are being recurrently used, but also their evolution reached a baseline where they are capable of matching or even overcoming some of other OFS. A simple configuration involving a PCF can be used to attain a robust and highly sensitive sensor. Besides, the clear advantage on manipulating and strategicaly modifying the design of a PCF allows to achieve a set of interferometers that can be used to monitor more than one parameter, characteristic that extol this type of OFS, enabling it to even surpass many of the current sensors [13]. Being a complex subject, propitious to spark off new physical properties, MOFs are still a matter of study by the scientific community.

Table 1.1: Figures of merit of some OFS based on PCFs and other sensing structures, namely FBGs, LPGs, singlemode fiber (SMF), thin core fiber (TCF), polarization maintaining fiber (PMF), 3 core fiber (3CF) and 7 core fiber (7CF).

Year	Structure device	Sensor length	Sensing principle	Measurand	Sensitivity	Ref.
2015	SMF-PCF-SMF	3 mm	MMI	Strain	$-3.16\,\mathrm{pm}/\mu\varepsilon$	[14]
2016	PMF+LPG	300 mm	SI	Refractive index	$-23.068\,\mathrm{nm/RIU}$	[15]
2017	3CF + LPG	60 mm	mode coupling	Curvature	$3.234\,\mathrm{nm\,m^{-1}}$	[16]
2018	SMF-PCF-SMF	150 mm	core mode coupling	Curvature	$10.89\,\mathrm{nm\,m^{-1}}$	[17]
2018	SMF-PCF	715 µm	FPI	Temperature	$15.61\,\mathrm{pm\,°C^{-1}}$	[18]
2019	SMF-TCF+ methylcellulose coating	2 mm	MI	Humidity	133 pm/%RH	[19]
2020	SMF-7CF-SMF+FBG	35 mm	Bragg reflection	Strain	$0.627\,\mathrm{pm}/\mu\varepsilon$	[20]
2020	SMF-PCF-SMF	500 µm	MZI	Strain	$1.97\,\mathrm{pm}/\mu\varepsilon$	[21]
2020	LPG-FBG	12 mm	Bragg reflection	Temperature Refractive index	$10\,\mathrm{pm\,°C^{-1}}$ 2326.7 nm/RIU	[22]
2020	SMF-(air gap)-PCF-(air gap)-SMF	3.3 mm	MZI	Refractive index	4629 nm/RIU	[23]
2020	SMF-PCF+hydrogel	140 µm	FPI	Humidity	81.05 pm/%RH	[24]
2020	FBG + graphene oxide coating	10 mm	Bragg reflection	Humidity	17.361 pm/%RH	[25]
2021	SMF-PCF	507 µm	FPI MMI	Strain Temperature	$2.5\,\mathrm{pm}/\mu\varepsilon$ $41.7\,\mathrm{pm\,°C^{-1}}$	[26]

1.2 Motivation and objectives

In modern society, sensors have a crucial role, being constantly applied in a wide variety of areas, comprising from scientific research to industrial purposes and health monitoring [27, 28]. The recurrent need of attaining simple sensors with higher reliability, and that could assure the current demands, led to an expansion on the search for new types of OFS that could measure physical, chemical, and biological parameters. The attractiveness of employing MOFs over the conventional fibers in the sensing design merged from the fact that a simple modification on its geometry structure would enhance new phenomena and could translate to a better performance on light guidance and consequently a higher sensitivity. Due to these particular characteristics, the usage of MOF sensors in several applications were and still are widely studied.

Nowadays, they are applied in a panoply of sensing areas, from the monitoring of mechanical and physical properties [13] such as strain, temperature, curvature, pressure, and refractive index, to the detection of biochemical samples [29], emphasizing gas detection [30]. The recent implementation of these sensors, which has been progressively studied, relies on their employment to detect and monitor aroma compounds, such as volatile organic compounds (VOCs) as well as organic compounds like glucose. These compounds are of great importance in several applications, for instance, VOCs are extensively used in industrial processes, on household products, and even in the alimentary industry [31, 32], however, they can be very dangerous and a threatening element, not only to the environment, in many cases causing frightful environmental hazards, but also to human's health, leading to severe adverse effects [32]. Due to this, VOCs detection has become an important issue and a matter of concern. On the other hand, organic compounds like glucose play a vital role in many fields such as in medical diagnosis and as quality monitor in the food industry [26]. Therefore the yearning of unveiling new PCF sensors that can match or even overcome the existing ones in the detection of these elements urges.

Over the past few years, the implementation of some PCF sensors in the measurement of these compounds has been reported, yet, the majority of them rely on an intrusive technique where the liquid or gas is inserted within the PCF, making this sort of procedure a complex one. With this, the objectives of this work are settled into learning and creating several OFS, using a newly designed PCF, fabricated at the Leibniz Institute of Photonics Technology (Leibniz-IPHT) in Germany, as an inline sensing structure. The first main objective relies on detecting organic compounds, where the monitoring of glucose solutions with different concentration, in a temperature varying medium, is proposed. The second main objective is to detect aroma compounds, specifically VOCs, being, therefore, proposed the monitoring of the evaporation process for different solutions of aqueous ethanol. Finally, one intends to evaluate the physical and mechanical properties of the sensor, by monitoring all the interferometric phenomena that underlie the sensor, and exploring its viability as an implementation of a multiparameter sensor.

1.3 Main contributions

D. Pereira, J. Bierlich, J. Kobelke, K. Wondraczek, M.S. Ferreira, "Monitoring evaporation of ethanol-water mixtures using a hollow square core fiber", in *Optical Sensors and Sensing Congress*, 2021.

D. Pereira, J. Bierlich, J. Kobelke, M.S. Ferreira, "Double antiresonance fiber sensor for simultaneous measurement of curvature and temperature", *Sensors*, 2021 [Submitted].

1.4 Thesis outlook

This thesis is divided in five chapters, where the characteristics of PCFs and the inner properties of the hollow square core fiber (HSCF) are studied.

In this first chapter, an overview of optical fibers is introduced. It is explored, with some special attention, the PCFs and their use as optical sensors, and compared with other types of OFS. A brief motivation regarding the use of PCFs is also presented, along with the structure of this work.

In the second chapter, a theoretical description about the types of PCFs and their guidance mechanisms is provided. Furthermore, a theoretical and simulation analysis is done on the guidance mechanisms of the HSCF used in this work.

In the third chapter, is presented a characterization of the HSCF in different liquid media, namely in glucose-water solutions and ethanol-water solutions, where a refractive index characterization is established, and the evaporation process is monitored.

In the fourth chapter, is done a characterization, for all components of the HSCF, in the air. Two broadbands were analyzed, and different parameters, such temperature, strain, and curvature were monitored.

In the fifth chapter, some final remarks are stablished and some future work suggestions are provided.

2. Photonic crystal fibers: main characteristics

2.1 Introduction

The need of attaining waveguides with specific optical properties led to a huge development of optical fibers. Among the new photonic crystal materials merged a new class of optical fibers, namely the PCFs. The PCF is a waveguide that is characterized by having periodic arrangements of air holes disposed along the entire fiber length, centered on a hollow core, being thus designated as hollow core PCF (HC-PCF), or centered in a solid core, being designated as solid core PCF (SC-PCF) [7]. The HC-PCF presents an air hole as core and is surrounded by a microstructured air hole cladding, while in the SC-PCF it is inserted a central defect on the MOF (absence of a hole) that constitutes the core [33]. Additionally, and besides the geometry, the MOFs are quite distinguishable from the traditional fibers in terms of the physics behind the mechanisms of light confinement. On the fabrication of a standard optical fiber, there are only few degrees of freedom (*e.g.*, the diameter) whose manipulation allows establishing some of the yearn properties. On the other hand, the MOFs design employs a wide number of degrees of freedom, for instance, one can choose the number of rings of air holes, the diameter of the air holes (d_h), and the distance between them (Λ) [11]. In addition to this, the choice of the material makes this sort of fiber a very versatile one upon managing properties like dispersion, nonlinearities, birefringence, and many others, opening up a wide number of applications that this may exert on optical systems [34].

2.2 Guidance mechanisms

On PCFs, light can be potentially guided by three principles, the MTIR effect, the PBG effect, and through the IC effect. Each of these effects happen when the necessary conditions are presented, not only in terms of geometry but also the material that composes the fiber, namely the core and cladding.

2.2.1 MTIR effect

Analogously to the standard fibers, on PCFs light can be guided due to the index guiding effect. That is, electromagnetic waves are confined within regions of a higher refractive index than the surrounding medium. Therefore, if the core's refractive index is higher than the cladding, then the necessary conditions are given to guide light. This can be achieved through SC-PCFs.

Unlike typical fibers, PCFs do not have a core and cladding with well defined boundaries. The preform fabrication stage of a PCF consists on a process of stacking cappilaries around a solid rod, knowned as the stack-and-draw process [35]. With this, along the entire fiber there will be a periodic array of air holes embedded within the silica material, generating a microstructured cladding. The periodic structures of air holes are employed to form an effective low index cladding around the core. Though one might consider that the air holes inserted within the cladding would create a geometrical average of the refractive index lower than the core, that is not entirely accurate. In fact, in the limit of long wavelengths ($\lambda >> \Lambda, d_h$) the cladding can be considered as an homogenous material with an average refractive index, n_{av}, of the materials that constitute the microstructured cladding, as [9]:

$$n_{\text{av}} \rightarrow \sqrt{(1-F)n_{\text{Si}}^2 - Fn_{\text{a}}^2}, \tag{2.1}$$

where F is the air-filling fraction and n_{a} and n_{Si} are the respective refractive indices of air and the silica glass that constitutes the fiber matrix. As $n_{\text{av}} < n_{\text{Si}}$, the PCF acts like a conventional fiber and thus light guidance will be established by a mechanism similar to TIR effect. However in the short wavelength range ($\lambda \sim \Lambda, d_h$), light does not see the microstructured cladding as an homogenous material, distinguishing the silica regions from the air holes. In this case, light will be strongly reppeled from the air holes by the TIR effect hence remaining confined within the core and being guided [9, 36]. Thus, this sort of fibers stand at least one guided mode.

The fibers that transmit light over the MTIR effect are commonly designated as index guiding fibers, and they can be categorized according to certain subclasses, where fibers are known to present a specific integrated characteristic that leads to the appearence of certain phenomena. Amidst those fibers highlights the high numerical aperture PCFs, the large mode area PCFs, and the highly nonlinear PCFs [37].

2.2.2 PBG effect

In contrast to the MTIR, the PBG effect can lodge light in a core with a lower refractive index, where the TIR effect cannot occur [7]. The PBG effect may be achieved in periodically structured materials, namely the photonic crystals, that have a periodicity on the scale of the optical wavelength [8]. Optical fibers based on the PBG effect comprise regular and periodic arrays of alternating elements in the cladding of high and low refractive index that creates optical bandgaps wherein no optical state is allowed. Only modes at wavelengths within the bandgap can propagate on the core. Therefore, light with wavelengths corresponding to the bandgaps cannot escape the core, being guided along the fiber with low loss. Also, the bandgaps prevent that the core mode couples to the cladding, as this last does not support any guiding mode [38]. Therefore, the cladding may exhibit both regions with photonic states, and subsequently propagating modes, and regions where there is a gap on propagating modes. It is the absence of cladding modes that prevents the propagating mode from leaking out of the core and coupling to the cladding.

The PBG effect mainly occurs on HC-PCFs, where the TIR effect does not have the necessary conditions to happen. However, and important to note, that it is reported on the literature cases of some PCFs that presented a solid core, namely the all solid PCFs, and the hybrid PCF, where light was guided by the PBG effect, or used both MTIR and PBG effect to lodge light within the core [33]. Among the HC-PCFs one highlights the subclasses such as the low index core fiber, the Bragg fiber and hollow core fiber [37].

2.2.3 IC effect

The IC effect is a recent guiding mechanism that has been proposed to explain the transmission of light in Kagomé fibers [39]. Unlike the PBG, in the IC principle the cladding does not present gaps wherein cladding modes cannot exist, meaning that light could escape from the core. Though the cladding is not void from propagating modes, it is verified that in certain wavelengths the core mode does not couple to the cladding, propagating with a relatively low loss [40]. Thus, both core modes and cladding modes can coexist with the same effective index, and therefore propagating constant, without significantly interact with each other. This is due to a low density of photonic states [39, 41]. Besides, the low overlap integral between the core and cladding modes is exceedingly reduced due to the large transverse phase mismatch between the slowly varying core modes and fast phase oscillations of the cladding modes [41, 42], therefore accentuating the coupling inhibition. In this process, the antiresonance (AR) effect is crucial since it imposes a reduction on the overlap integral, easing the IC [43].

The PCFs that rely on this guidance mechanism usually operate under AR effect, therefore they are known as antiresonant hollow core fibers (ARHCF) [44]. This type of fibers have strongly gained the attention by the scientific community, due to their notorious properties that have edge over other PCFs, such as ultra-low loss and strong confinement of light [44, 45]. Among the ARHCFs' class highlights the Kagomé fibers, the pioneers in the discover of the IC guidance, the negative curvature fibers, such as the revolver fibers and the hexagram fibers, where it is the negative curvature of the core that inhibits the coupling [43], and the simplified antiresonant fibers, such as the capillary fibers and the double antiresonant fibers. These last, present a dual AR mechanism, each with dissimilar responses. The HSCF used in the framework of this thesis is a notorious example of this last category.

Figure 2.1 exhibits a schematic diagram of some distinctive PCFs that have been proposed. Their classification was done taking into account the known guidance mechanism, and following the respective literatures [37, 43].

2.3 Losses

An optical fiber is an eximious guide that allows light to travel through a considerable distance without being compromised by certain external factors, however, it is subjected to certain features that can cause significant losses in light guidance. Throughout the years

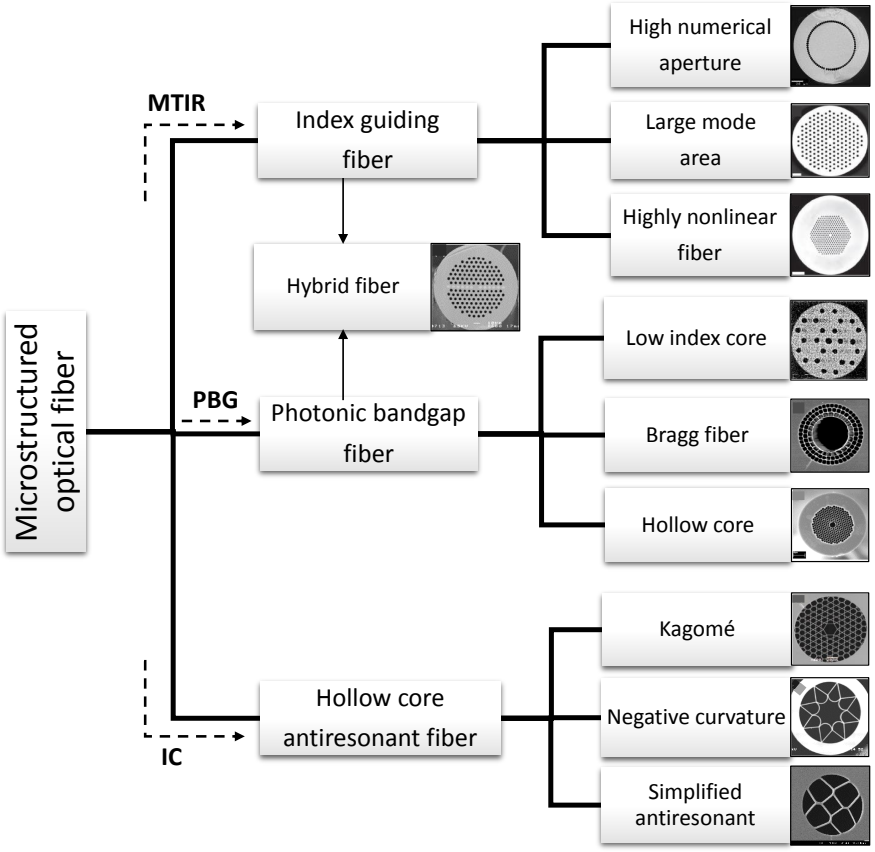

Figure 2.1: Diagram of the different classes of MOFs established according to the guidance mechanism.

PCFs were highly developed and the tremendous losses they initially presented have been considerable decreased. Still, it remains an important factor to take into account.

Similarly to the conventional fibers, the attenuation of the light power in PCFs may be caused by material absorption, where in silica materials, the phonon vibrations and the hydroxid absorption are the major responsibles for inducing losses. The Rayleigh scattering also contributes to the attenuation increase. This event comes down to the scattering of light by atoms or molecules of size much smaller than the lights wavelength [5], and arises from density and compositional fluctuations originated from irregularly spaced atoms in the lattice structure that merged during the fiber manufacture [46]. In addition to these losses, MOFs present another one, namely the confinement loss (C_L) or leakage loss, which is given by [47]:

$$C_L = \frac{40\pi\Im(n_{\text{eff}})}{\ln(10)\lambda}, \tag{2.2}$$

where $\Im n_{\text{eff}}$ is the imaginary component of the effective refractive index. Ideally, in both SC-PCF and HC-PCF, the air holes inserted into the material matrix should be continuously prolongated to infinity, in order to prevent the core modes leakage to the cladding [10, 48]. However, since the microstructured cladding is finite, there will always be losses due to the

leakage of the core modes, meaning that the energy of the propagating mode will decay along the fiber. Thus, the propagating modes in PCFs are known as leaky modes. These losses happen in any optical fiber, though in HC-PCFs, where the HSCF is included, the greatest cause of impoverishment on the optical power of light may be stricted to confinement loss or certain variations in the fiber structure along its length. Both absorption and Rayleigh scatering have a small impact since light is guided in air and not in the material [10].

2.4 Hollow square core fiber

The HSCF used in this work, whose cross-section is shown in figures 2.2a and 2.2b, is a HC-PCF that presents a squared shape core surrounded by four identical air petal shape structures intercalated with four interstices. The size of the core is ≈11 µm and it is surrounded by silica strands of 1.7 µm of thickness. The air structures arrangement extend a diameter of 52 µm, and around these there is a silica cladding with width of 36.5 µm. The fiber's outer diameter matches the 125 µm of the singlemode fiber (SMF). Notice that in the following of the work, the designation of cladding of the HSCF will be established for the whole geometry that is beyond the hollow core.

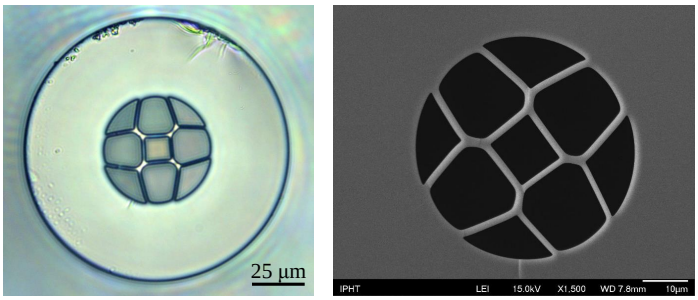

(a) (b)

Figure 2.2: Images of the HSCF in a transversal perspective (a) using a microscope (400×) and (b) using scanning electron microscopy.

2.4.1 Sensor design

The layout of the sensor used in this work was based on an inline configuration where the HSCF was spliced between two segments of SMF. The splicing process was executed with a Fujikura 40S splicer, which was operated in the manual mode, allowing the alignment between fibers to be personalized by the user. Given the geometry of the HSCF and the fragility of the microstructures of the fiber, it was necessary to adjust the parameters of the splicing program so that one could attain an equilibrium between the splicing strength and the integrity of the PCF structure. To keep the cohesion of the microstructures intact, the arc was discharged mainly on the SMF instead of the limits of the SMF and HSCF, as the scheme in figure 2.3a illustrates. This, in turn, appeared as a challenge since the splicing resistance is slightly compromised, making it necessary to alter the arc parameters to overcome this issue.

Those parameters were found making several attempts on modifying both the arc discharge power and duration. The parameters that were achieved to produce a reasonable sensor required an arc discharge time up to 500 ms, and a power up to 12 arb. units. Notice that in an automatic splice the standard parameters are set to 2000 ms and 20 arb. units. Above the found values, significant deformations in the HSCF were enhanced, as it is perceived in figure 2.3b (top).

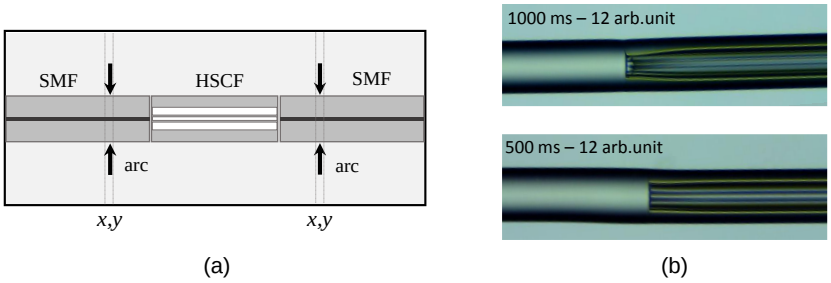

Figure 2.3: (a) Scheme of the splicing process of the HSCF between the SMFs. The dark arrows represent the location in which the arc was discharged. (b) Microscopic pictures of the HSCF splice when the splicing parameters are set to 1000 ms and 12 arb. units (top), and 500 ms and 12 arb. units (bottom).

2.4.2 Operation principles

In the HSCF, light is guided within the air core through the AR reflection. However, depending on the incident angle and incident area, as well as the fiber length, light can also propagate through the silica structures that surround the core, as one can observe in figure 2.4, where a simulation of the core modes and cladding modes was done for a wavelength

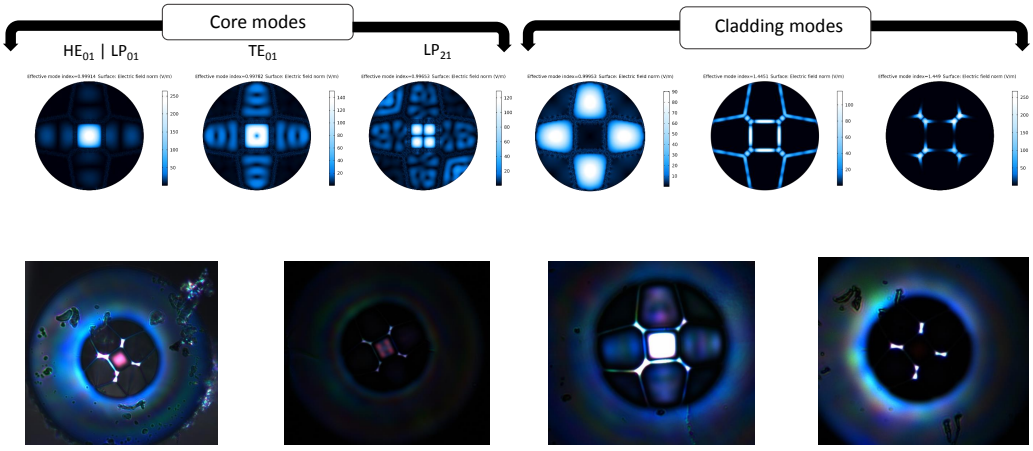

Figure 2.4: Simulation of the core modes, HE_{11}, TE_{01} and LP_{21} and some of the cladding modes at 650 nm (top). Micrographs of light propagation in the HSCF, taken at the Leibniz - IPHT (bottom).

of 650 nm, by resorting to the finite element software COMSOL Multiphysics (version 5.6). The simulation results are in agreement with the propagating modes that are experimentally

observed, also in figure 2.4. The propagation of the numerous modes on the distinct regions of the fiber makes it possible for a new set of events to happen, especially interferometric phenomena. The interference of light is based on the superimposing of two or more light beams, with the same frequency, that present a phase difference. That phase difference is usually originated due to the difference of optical paths in light guidance, leading to constructive and destructive interferences that create a pattern. In the guidance of light of the HSCF sensor, two different interference phenomena may occur, namely the MZI and MMI. Those interference mechanisms are highly sensitive to the surrounding medium, making this type of fiber excellent for sensing purposes. With this, in this section one will introduce all of the phenomena that happens within this particular MOF, making a brief discussion on its physical properties.

2.4.2.1 AR

The AR principle can be described by the antiresonant reflecting optical waveguide (ARROW) model, which expresses the optical fiber as an array of high and low refractive index layers, and where the former act as Fabry-Perot (FP) resonators [49]. In short, the wavelengths that do not obey the resonance condition are reflected within the resonator, and thus propagate along the fiber core. However, wavelengths near the modal cutoff condition escape the FP resonator, being posteriorly lost. Therefore, for certain guidance windows there will be certain narrower high loss frequency bands where some notorious depression peaks are visible. The wavelengths in which those peaks are located are designated as resonance wavelengths (λ_m), and follow the resonance condition [50]:

$$\lambda_m = \frac{2w\sqrt{n_{\mathrm{Si}}^2 - n_{\mathrm{a}}^2 \sin^2(\theta)}}{m}, \tag{2.3}$$

where w is the thickness of the FP resonator, θ is the incident angle, and m is the resonance order. Notice that for the AR guidance, the reflections present glancing angles, therefore $\sin(\theta)$ can be approximate to the unit. In the particular case of the HSCF, there are two distinctive AR guidance mechanisms, namely an internal AR, where light is trapped in core and surroundings of it, and the external AR, wherein light remains confined by the outer cladding region. Figure 2.5 illustrates the light propagation in the fiber that originates these two ARs. The light that propagates in the air core, when encountering the interface between the core and the silica strands, will be both reflected, thus remaining in the air core, and refracted to the silica strands. The silica strands will be acting as a FP resonator (FP_1 resonator in figure 2.5), which means that for the AR wavelengths light will be reflected within the resonator and refracted back to the core. The internal resonance (IR) occurs when the resonance wavelengths escape the resonator and leak to the air structures, as they are further lost in the propagation [51]. In the external AR guidance, light leaks from the core, and thus may propagate in the petal air structures and interstices that surround the core. There, light will also be refracted to the outer silica cladding section, which, in turn,

will also act as a FP resonator (FP_2 resonator in figure 2.5). Therefore, an external resonance (ER) is expected to occur for the resonance wavelengths, where these will leak out from the fiber.

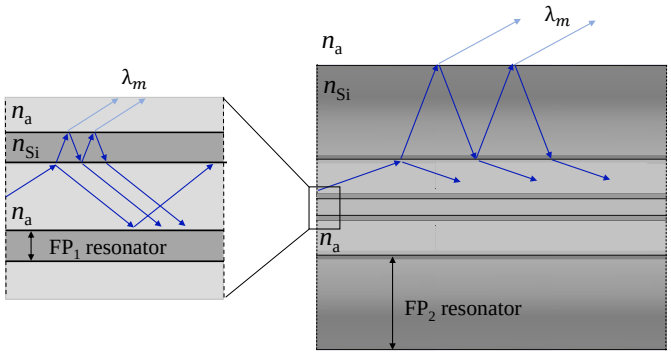

Figure 2.5: Scheme of the optical paths of light in the internal AR guiding process, which occurs in the core area, and the external AR, that occurs in the outer cladding section.

For a better perception of these effects, figure 2.6a presents the spectral response of a 7.50 mm HSCF sensor that was acquired in the air, under the normal conditions of temperature and pressure, and in figure 2.6b the respective curve when a low pass filter is applied. The low pass filter of $0.05\,\mathrm{nm}^{-1}$ was applied to reduce the noise associated with the raw

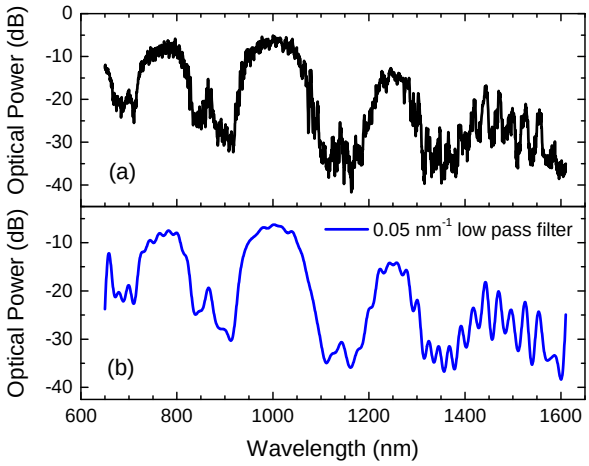

Figure 2.6: (a) Transmission spectrum of a 7.50 mm HSCF sensor and (b) the respective spectrum when a $0.05\,\mathrm{nm}^{-1}$ low pass filter is applied.

acquired data, and thus, to allow a better visibility of the AR guidance modulation. Analyzing the spectrum two behaviors stand out immediately. First, one sees the broadbands, centered at ∼760 nm, ∼990 nm, and ∼1230 nm, where light is transmitted with relatively low loss, and the neighbouring high loss widebands that correspond to the resonance frequencies of inner silica strands. Secondly, at higher wavelengths (starting ≈1270 nm) one sees with more detail the recurrent dips that modulate the signal, being these respective to the ER. The comprehension of these two mechanisms that modulate the transmitted optical signal re-

lies on understanding the modal propagation in the HSCF. Therefore, to further understand those, particularly the internal AR, it is necessary to comprehend the propagation of the fundamental mode (HE_{11}) as well as its intrinsic properties. Considering the perturbation theory model, encountered in [52], the effective refractive index of a propagating mode is described by the expansion:

$$n_{\text{eff}} = n_a(1 - a\sigma^2 - b\sigma^3 - c\sigma^4 + id\sigma^4), \tag{2.4}$$

where σ is denoted as the perturbation parameter and is invertionally proportional to the core wavenumber, k_{a}, and the core radius r. The core wavenumber is related with the vacuum wavenumber, k_0, through $k_{\text{a}} = k_0 n_{\text{a}}$. The coefficients a, b, c, and d are real numbers and can be described by the real coefficients of the radial wavenumber, k_1, k_2 and by the complex coefficient k_3. With this, it is possible to establish the following correlations [52]:

$$a = \frac{k_1^2}{2} = \frac{j_{m-1,n}^2}{2}, \tag{2.5a}$$

$$b = k_1 k_2 = \frac{j_{m-1,n}^2(\epsilon+1)\cot(\phi)}{2\sqrt{\epsilon-1}}, \tag{2.5b}$$

$$c = \frac{k_1^4}{8} + \frac{k_2^2}{2} + k_1\Re(k_3) = \frac{j_{m-1,n}^4}{8}c_0 + \frac{j_{m-1,n}^2}{2}c_1, \tag{2.5c}$$

$$d = -k_1\Im(k_3) = \frac{j_{m-1,n}^3}{2}\frac{(\epsilon^2+1)}{\epsilon-1}(1+\cot^2(\phi)), \tag{2.5d}$$

where c_0 and c_1 are given by:

$$c_0 = 1 - \frac{(\epsilon-1)}{m}\cot^2(\phi), \tag{2.6a}$$

$$c_1 = \frac{(4-2m)(\epsilon+1)^2}{4(\epsilon-1)}\cot^2(\phi) - m. \tag{2.6b}$$

The variable $j_{m-1,n}$ represents the n^{th} root of the Bessel function $m-1$, for the hybrid mode $HE_{m,n}$. ϕ is the accumulated phase between two consecutive reflections of a ray in the silica glass structure, and the parameter ϵ is the square fraction of the refractive indices of the silica glass and air, respectively. Developing the set of equalities from equations 2.5a to 2.6b, one concludes that:

$$n_{\text{eff}} = n_a - \frac{j_{m-1,n}^2}{2k_0^2 n_a r^2}\left(1 - \frac{(\epsilon-1)\cot(\phi)}{\sqrt{\epsilon-1}k_0 n_a r}\right) + i(\cot^2(\phi)+1)\frac{j_{m-1,n}^3(\epsilon^2+1)}{2(\epsilon-1)k_0^4 n_a^3 r^4}. \tag{2.7}$$

Based on the analytical equation 2.7, a complex effective refractive index is attained, where the real component describes the spectral tendency of the leaky mode effective index, while the imaginary part is associated with the losses inherent to the mode propagation. Given this, the spectral propagation of the HE_{11} mode was simulated using COMSOL Multiphysics. The real and imaginary components of the effective index of the mode obtained by the simulation are

represented in figures 2.7b and 2.7c. It is quite notorious the asymptotic behaviour of the real part of the effective index. In fact, this behavior is highly characteristic in ARHCFs, where the asymptotic curves tend to a specific wavelength, the so-called resonance wavelength. This fact is also proven by the behavior of the imaginary component of the refractive index, where high intensity peaks are notoriously located in the same frequencies as the asymptotic wavelength, and by comparing these frequencies with the wavelengths of higher losses in the transmission spectrum (figure 2.7a). Additionally, using the real part of the effective index, one compared

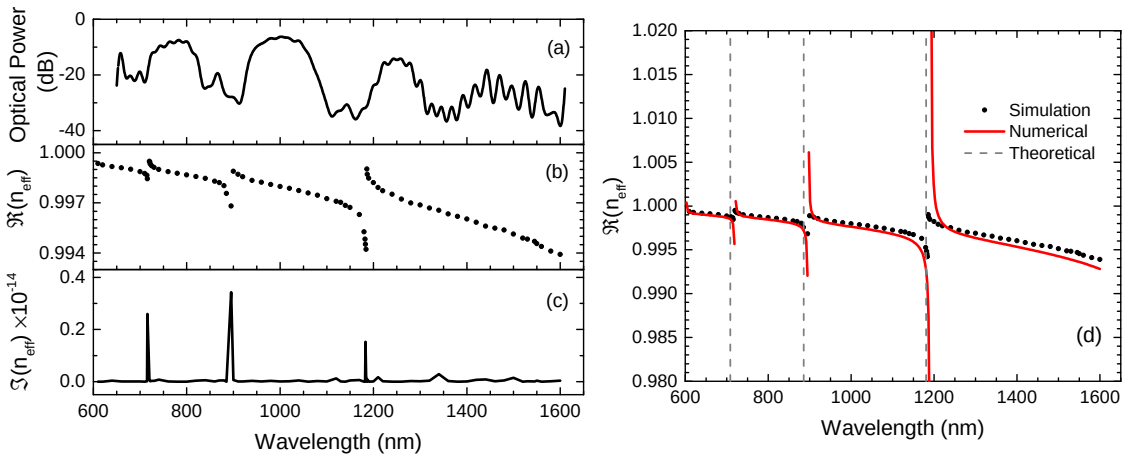

Figure 2.7: (a) Experimental transmission spectrum of the HSCF sensor. (b) Real component and (c) imaginary component of the effective refractive index with wavelength attained by the COMSOL Multiphysics. (d) Real effective refractive index attained by the COMSOL Multiphysics (Simulation), and by equation 2.7 (Numerical). In dash lines is represented the expected frequency of the IR, according to equation 2.3.

the simulated values with the ones obtained by the analytical equation 2.7 (figure 2.7d), verifying a good agreement between both, validating, therefore, the use of equation 2.7 to describe the resonance within the HSCF. To further corroborate the established analysis, the theoretical values of the IR wavelengths, foretell by equation 2.3, were also represented in figure 2.7d. A good match between the simulated and the theoretical resonance is perceived, although there is a small shift between the theoretical and numerical resonance wavelengths. This can be justified by the simplified geometrical approximation used in the numerical model. However, in an overall perspective the numerical equation describes this fiber with a relatively good accuracy. The imaginary components of the simulated effective index of the mode and the analytical equation, illustrated in figures 2.8a and 2.8b, shows a correspondence in the frequency in which the intensity of the refractive index becomes higher. However, a notorious difference in the magnitude of the index is noticeable. This may be explained considering the dependence of the losses associated with the mode confinement, *i.e.*, the imaginary component of the effective refractive index, with the fiber structure. That is, the more microstructures are surrounding the core, the better confined the mode will be [53]. On the numerical simulation, only the inner structure of the fiber was considered (figure 2.8c), and since the confinement of the leaky mode is increasingly accentuated with the quantity

of material that surrounds the core, then, a sudden decrease on the losses due to leaking is expected. On the analytical equations, a model of a capillary constituted only by an air core, a glass ring, and a minor air cladding was considered (figure 2.8d), therefore making it viable

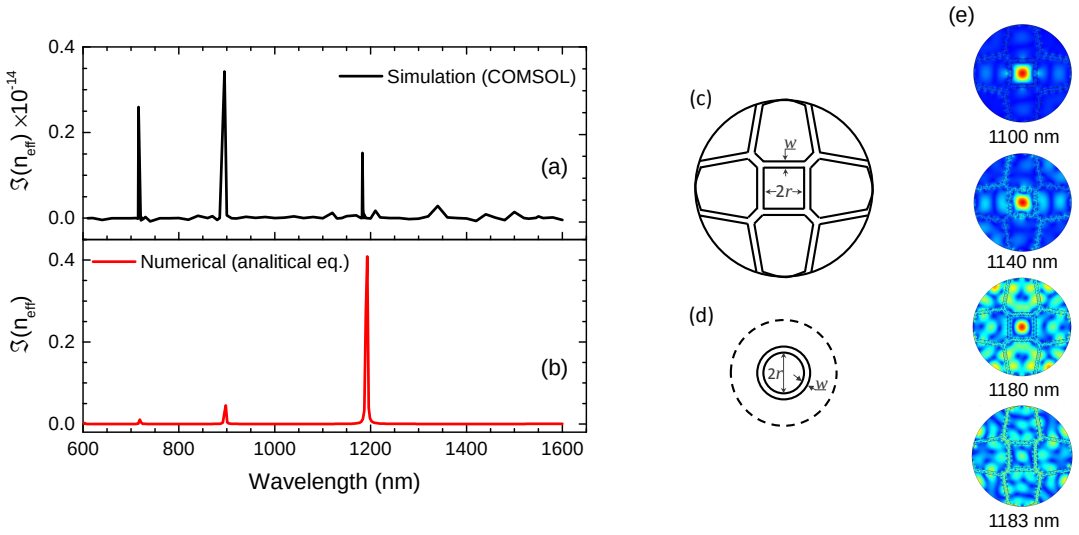

Figure 2.8: (a) Imaginary effective refractive index of the HE_{11} mode attained by the COMSOL simulation, and (b) by the analytical equations (numerical). (c) Geometrical model of the HSCF used in the simulation, and the (d) geometrical model of the capillary tube used in the analytical study. (e) Sequence of the electric field profile of the fundamental mode at wavelengths of 1100 nm, 1140 nm, 1180 nm and 1183 nm.

for more losses associated with the mode leakage. A simple test to prove this concept would be to simulate merely the core of the HSCF surrounded by the silica strands, disregarding the neighbouring air structures with the remaining strands. Another possible reason may be due to the low wavelength resolution used in the simulation. That is, the expected resonance wavelength may not have been reached, and therefore the losses had not met its maximum value. The compensation of this problem would be difficult to overcome since the electric mode distribution is more dispersed in the cross section of the fiber, as figure 2.8e shows, and may lead to inadvertly mistaken the mode with other virtual solutions. Therefore, in terms of heuristical usage one will consider the analytical approach for the analysis of losses in the HSCF.

Considering the previous discussion, and given that the imaginary component of the effective index of the leaky mode attained in the simulation is highly susceptible to the region of interest, this element serves the solo purpose of qualitative analysis, where one intends to show the general good concordance between the model of the HSCF that was simulated with the analytical equations of an ARHCF, and should not be used for quantitative analysis. With this, and since the $\Im(n_{\text{eff}})$ is related to losses existing in the mode, specifically in the mode confinement, one can estimate the expected transmission window that is formed by the AR propagation, and consequently the expected transmission spectrum of the HSCF. Note that it was considered that the major factor that induces losses in the HSCF is the confine-

ment loss of the propagating mode. Other possible factors, like the bending and absorption losses as well as the Rayleigh scattering, are too small in HC-PCFs, and thus can be disregarded [10]. Moreover, it is important to notice that the use of equation 2.7 is not limited only to the IR, being its usage capable of also predict the ER. The IR is mainly resultant of the core mode leakage (HE_{11}), whilst the ER is mainly induced by the leakage of the cladding mode HE_{21}. Given this note, figures 2.9a and 2.9b present the numerical simulation attained for the ER and IR, respectively. The conjugation of these two resonances allows to predict the transmission spectrum of the HSCF (figure 2.9c). A normalization was carried out to the numerical results to better perform a comparison with the experimental transmission spectrum. In order to compare the simulated results with the experimental ones, a superpo-

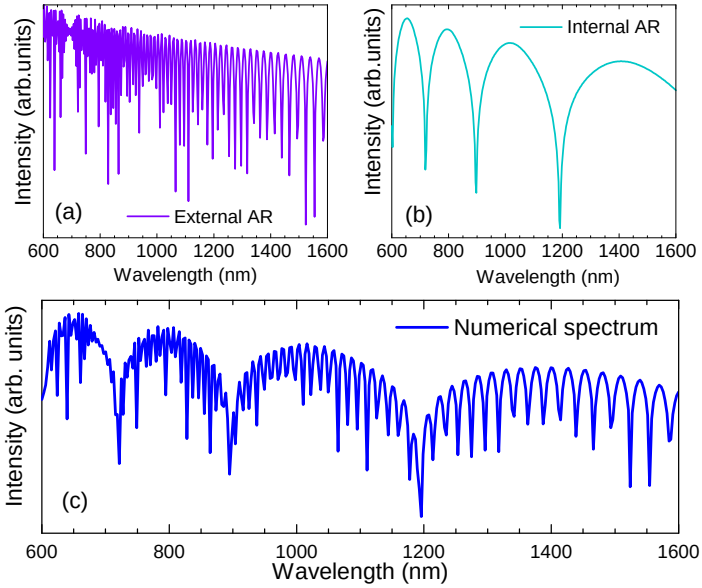

Figure 2.9: (a) Numerical solution of the external AR spectrum, and (b) the internal AR spectra. (c) Numerical solution of the transmission spectrum of the HSCF.

sition of both spectra was carried out, and is represented in figure 2.10a. To begin with, the resemblences on both results are quite notorious, in specific for the ER dips, as figure 2.10b depicts. From the experimental spectrum it was possible to distinguish the resonances from the 48^{th} to the 61^{st} order, located in the wavelength range between 1200 nm and 1600 nm. The high visibility of the ER in these frequencies suggests that this phenomenon is more propituous to occur in this range than in lower wavelengths. Moreover, it is important to perceive that the intensity of the internal AR bands decreases for higher wavelengths. The decrease of the optical signal for lower frequencies indicates that the core modes are not so well confined within the core region, meaning that the coupling of light to the cladding region will be favored. As result, the external AR will be further stimulated, leading to a notorious modulation on the transmission. The ER dip values achieved in the experimental and in the numerical transmission spectrum are represented in figure 2.10c, where the theoretical values, obtained by equation 2.3, are also shown. Although the results are similar, for higher resonance orders there is a slight deviation. This can be partly justified by the impact of the

internal AR guiding that attenuates this phenomenon, therefore leading to a higher difficulty in distinguishing the ER, as well as to the noise associated to the transmission spectrum, that could overshadow near resonance peaks. Furthermore, in figure 2.10a it is also possible to in-

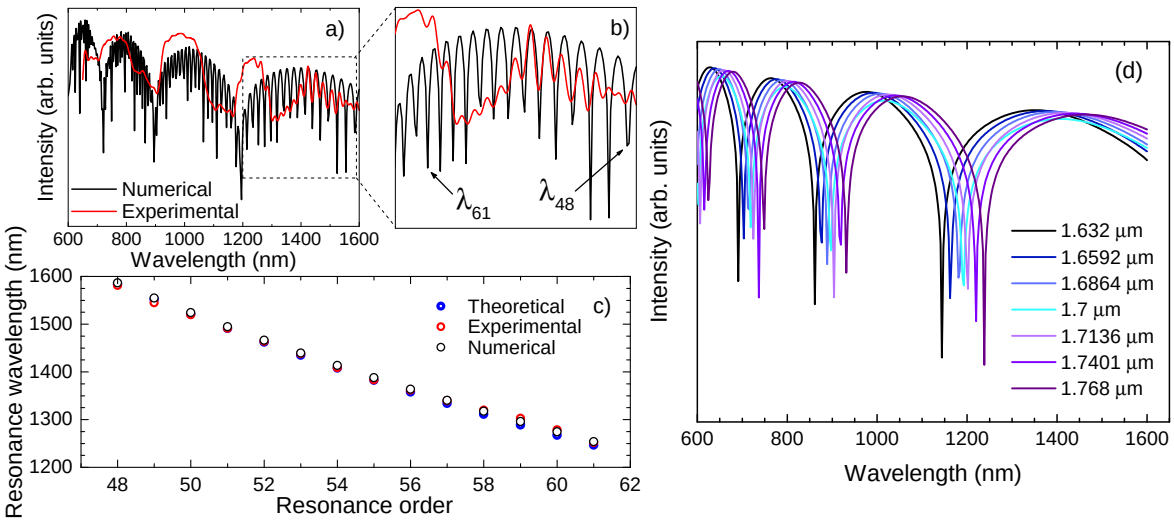

Figure 2.10: (a) Representation of the simulated and experimental transmission spectrum of the 7.50 mm HSCF. (b) Zoom-in of the transmission spectra in the range of 1200 nm-1600 nm, where the external AR modulation is observable. (c) Values of the ER dips attained from the numerical and experimental spectrum, and the theoretical values from equation 2.3. (d) Representation of the simulated internal AR spectra for different values of w.

fer that similar low loss broadbands were attained in both experimental and numerical cases, however, the high losses broadbands, respective to the IR frequencies, show some differences. The IR dips, which one would expect to occur in the surrounding silica strands of 1.7 µm, appear in the experimental procedure as broadbands instead of well defined peaks as the simulation predicted. However, one must be attentive to the fact that resonance frequencies obtained from the analytical equations are located within the range of the experimental resonance bands. That is straightforwardly justified by the fiber's irregularities, that is, the slight variations on the thickness of each strand that surrround the core, combined with possible fluctuations along the HSCF length. The fiber's dimensions, provided by the manufacturer, have associated a 5 µm marge error of the total fiber width, which means that the thickness of the inner silica strands may not be constant, varying in a margin of 4% above and below the measured value. Therefore, taking this variable into account and studying the impact of this imbalance, it is obtained in figure 2.10d the several spectra considering the width error margins. One observes a fast shift in the IR wavelength with a very small width variation. It is, therefore, reasonable to expect that the experimental resonance broadbands acquired are formed and mediated by the fiber's slight deformations.

2.4.2.2 MMI

The modal interference is associated with the superimposing of two or more distinct modes. Each guided mode has a particular electric field distribution as well as a specific propagation constant. Distinct modes have distinct propagation constants, meaning that they will travel at different speeds. Therefore, they will interfere. In the particular case of the HSCF sensor, this interference happens when the sensor is interrogated in transmission. The conditions in which the coupling of light between the SMF and the HSCF is done may not only excite modes within the HSCF's core, but can also stimulate the coupling of light to the HSCF cladding, as figure 2.11 illustrates. Hence, the cladding modes will interfere. The interfering light is then recoupled at the exit SMF. Mathematically describing the process, the difference

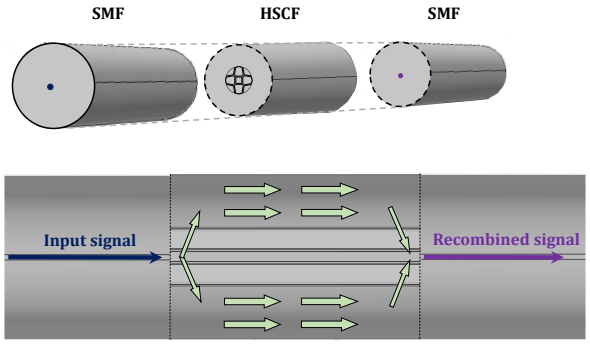

Figure 2.11: Schematic representation of the MMI on the HSCF. The fundamental mode of the SMF will excite multiple modes within the cladding of the MOF. Those modes will interfere, being posteriorly combined to the SMF.

in the optical path, Δr, will be:

$$\Delta r = L(n_{\text{eff}}^{\text{cl}_i} - n_{\text{eff}}^{\text{cl}_j}), \tag{2.8}$$

where L is the HSCF length, and $n_{\text{eff}}^{\text{cl}_i}$ and $n_{\text{eff}}^{\text{cl}_j}$ are the effective refractive indices of the i and j cladding modes. Due to the difference in the optical path between the modes, there will be an induced phase shift, $\Delta\phi$:

$$\Delta\phi = \frac{2\pi}{\lambda_{\text{MMI}}} L(n_{\text{eff}}^{\text{cl}_i} - n_{\text{eff}}^{\text{cl}_j}), \tag{2.9}$$

where the recombined signal in the SMF may be constructive if the phase shift is multiple of 2π, *i.e.*, $p2\pi$, with $p \subset \mathbb{Z}^+$. Through the simplified process that was described, one can see that certain parameters related to the specialty fibers will affect considerably the sensor performance upon measuring external changes. Among those parameters, the length of the sensing element, as well as the effective refractive indices of the cladding modes are some to take into consideration. In fact, such dependence can be given by [54]:

$$\Delta n_{\text{eff}}^{\text{cl}} = \frac{\lambda_2 \lambda_1}{(\lambda_2 - \lambda_1)L}, \tag{2.10}$$

where $\lambda_2 - \lambda_1$ is the difference between wavelengths of two adjacent peaks, and $\Delta n_{\text{eff}}^{\text{cl}}$ is the difference of the effective refractive indices of the interfering cladding modes.

It is quite well known from the literature that the PCFs are used for both detection and sensing of gases and liquids [55]. In fact, the use of the SMF-HSCF-SMF configuration potentiallyenhances the modal interference which is highly susceptible to the external medium changes. Since the event of MMI occurs within the outter cladding region, the interference of modes can be significantly changed when the fiber is presented to modifications on the outer medium.

2.4.2.3 MZI

For some particular transmission sensors, where a distinct type of fiber is spliced between two segments of a similar one, the interference between core modes and cladding modes usually takes place. In the case of the sensor in study, it is the specific configuration of the SMF spliced to both sides of the HSCF, allied to the size of the core, that enhances the coupling of light to the cladding structures. This favors the occurrence of a MZI.

The core mode of the SMF will be redistributed when reaching the interface of the HSCF. That redistribution will allow the presence of several modes on the HSCF core as well as the cladding. In figure 2.12, some of the simulated propagating modes within the core of the HSCF and the silica strands are represented, using the COMSOL Multiphysics, at an operating wavelength of 1570 nm. Since the cladding material is different than the core

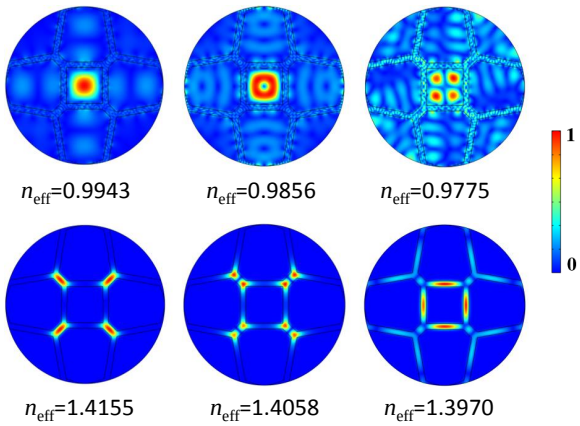

Figure 2.12: Simulation of the core modes (top), and the silica strand modes (bottom) in the HSCF, by using the COMSOL Multiphysics, for an operating wavelength of 1570 nm. Below the modes are represented their effective refractive index. The colorbar shows the normalized electric field intensity.

material, the conditions in which the modes propagate in each region will be dissimilar. This effect induces a phase shift between the core and cladding modes so that when they couple back to the SMF their recombination will result in an interference. A scheme of the MZI in the HSCF sensor is depicted in figure 2.13. The input eletromagnetic field will propagate in two sections of the fiber, a fraction of the light will propagate on core and another fraction

will propagate on the silica strands that surround the core. Given that light will experience

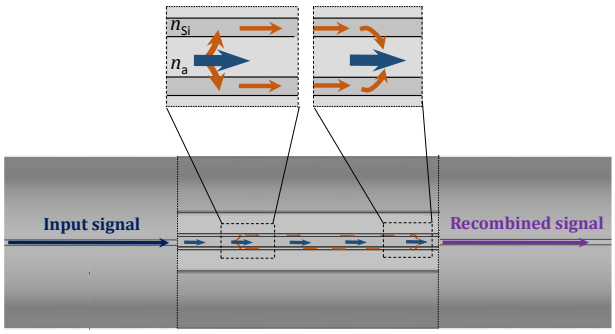

Figure 2.13: Schematic representation of the MZI on the HSCF. The fundamental mode of the SMF will excite multiple modes within the core of the HSCF where some are going to be couple to the silica strands, being later recoupled to the core and will interfere when they are combined to the SMF.

two media with different refractive indices (different speeds in each medium), a difference in the optical path is induced. This can be described by:

$$\Delta r = L(n_{\text{eff}}^{Si} - n_{\text{eff}}^{\text{a}}), \tag{2.11}$$

where n_{eff}^{Si} and n_{eff}^{a} are the effective refractive indices of the silica strands and the air core, respectively. The difference in the optical path of light will create a phase shift, which, for constructive interference gives rise to [54]:

$$\Delta n_{\text{eff}} = \frac{\lambda_1 \lambda_2}{(\lambda_2 - \lambda_1)L}, \tag{2.12}$$

where Δn_{eff} is the difference of the effective refractive indices of silica and air. Notice the duality of the expressions attained for both MMI (equation 2.10) and MZI (equation 2.12). Due to the MZI inner location in the fiber, the core and cladding modes will only be mediated by external parameters that directly affect the fiber structure or any of its optical properties.

3. Characterization in liquid media

In this chapter, a study on the sensor performance in two different liquid media was conducted, specifically in both glucose aqueous solutions and ethanol aqueous solutions. For the glucose aqueous medium, a detailed analysis to the refractive index was performed in a constant temperature environment, and in a temperature varying environment. As for the ethanol aqueous medium a study on the evaporation profile was carried out.

3.1 Study of glucose-water mixtures

The main objectives of this section of the work consisted on calibrating the HSCF sensor to the adequate operating wavelength, followed by a detailed analysis on the sensor response to the refractive index. A comparison between the sensor's performance and some sensors reported in the literature was made. The resolution of the sensor was also addressed. Moreover, a temperature independent refractive index detection was performed, and the thermo-optic coefficients (TOC) of the glucose solutions were determined.

3.1.1 Refractive index measurements

To evaluate the sensor response to variations on the external medium refractive index of the medium, the HSCF was subjected to solutions of glucose with different weight concentrations (wt.%). A series of deionized water-glucose mixtures were prepared under a controlled laboratory environment and stored for 24 hours to allow their stabilization. The mixtures had different weight fractions of glucose, starting at 0 wt.% up to 50 wt.%, in steps of 2.5 wt.%. After the stabilization period, the refractive index of each solution was measured using an Abbe refractometer (KRÜSS optronic refractometer) operating at 589 nm. The spectral response

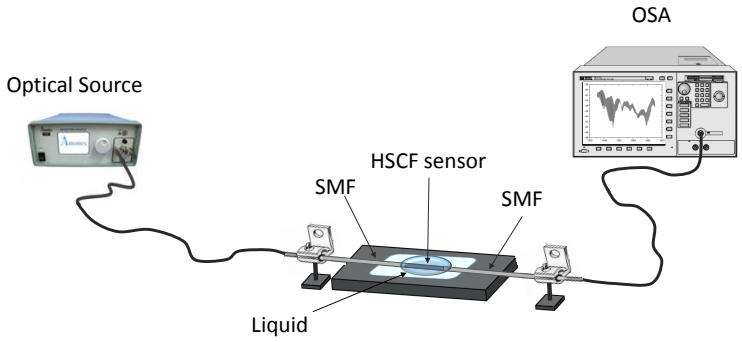

Figure 3.1: Experimental setup used on the refractive index measurements.

of the sensor was observed in a transmission configuration, where a broadband optical light

source (Amonics, model ALS-CL-17-B-FA) centered at 1570 nm, with a bandwidth of 80 nm, and the optical spectrum analyzer (OSA, Anritsu MS9740A) were used. Figure 3.1 illustrates the experimental setup used. The attained results for the refractive indices measured for each solution, using the refractometer, are represented in figure 3.2a, where a linear tendency on the increase of the refractive index with an increase in the concentration of glucose is observed. To ascertain the correct preparation of the solutions one proceeded to compare the experimental results with the ones already established in the literature [56]. Both curves are

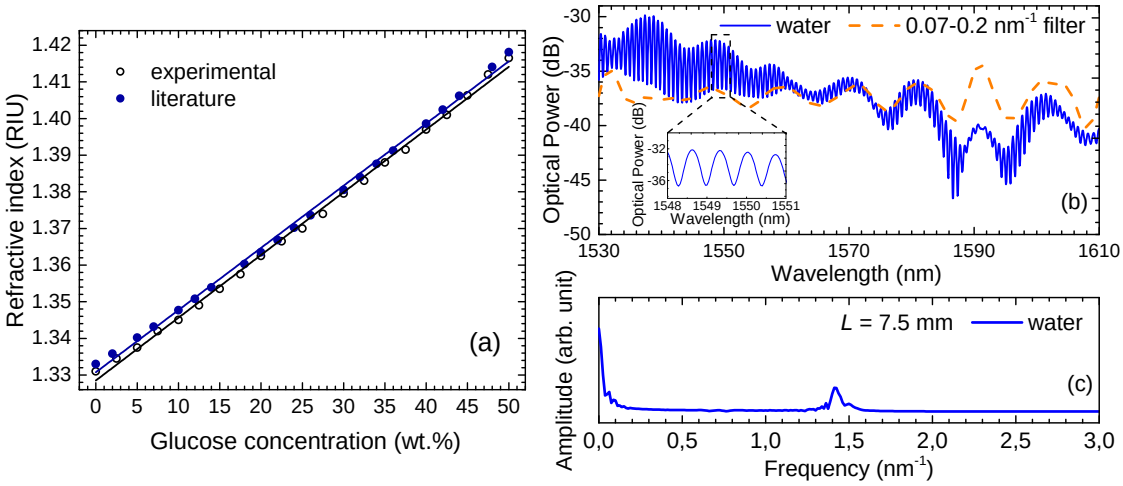

Figure 3.2: (a) Refractive indices for different mass fraction solutions of glucose experimentally measured with an Abbe refractometer ($\lambda = 589$ nm), compared with the values obtained from the literature [56], at room temperature of 20 °C. (b) Spectrum of the HSCF sensor of 7.50 mm immerse in water with the band pass filter of 0.07-0.2 nm^{-1} used to monitor the MMI component. (c) FFT obtained for the same sensor for the same medium.

very much alike, having a small shift between them, reason that can be explained by the fact that the room temperature may have not been 20 °C. The sensing head was constituted by a 7.50 mm long of HSCF spliced between two sections of SMF. The spectral response of the sensor when surrounded by water is represented in figure 3.2b, as well as the bandpass filter applied (0.07-0.2 nm^{-1}). The spectrum presents two main frequencies, a higher frequency that is modulated by a lower frequency, as evidenced by the fast Fourier transform (FFT), in figure 3.2c. There is a central peak at higher frequencies, approximately at 1.422 nm^{-1}, and an aggregate of small frequencies from the DC component up to 0.15 nm^{-1}. Recalling the description made about the principle of operation of the HSCF, in the subsection 2.4.2, the two AR mechanisms were described, as well as two interferometers, the MMI and MZI, that may take place within the fiber. Because the sensor was tested within the range of frequencies of the C band, no IR occurs in this window. As for the ER, its monitoring also reveals to be not viable in these experimental conditions. When the HSCF is merged in a liquid medium, the resonance condition is slightly modified. As the liquid refractive index is closer to the refractive index of silica, the ER dips visibility decreases and the MMI becomes more dominant over this, and thus the ER will fade away. Consequently, only the MMI and MZI are expected to be observable. Therefore, the high frequency that is perceptible in

the sensor's response in figure 3.2b and its inset, corresponds to the MZI modulation while the low frequency to the MMI. Notice that this is also proved by the simulated modes, that were represented in figure 2.12, and whose interference originates the high frequencies that range from the $1.225\,\mathrm{nm}^{-1}$ to $1.333\,\mathrm{nm}^{-1}$. Since the MZI is spectrally expressed on a high frequency domain that is modulated by a low frequency (MMI), it is necessary to separate both components to analyze them individually.

However, before proceeding to the individual analysis of each interferometric component to the glucose solutions, one must not forget that the measurements of the refractive indices of the glucose solutions were carried out using a refractometer that operates at a wavelength of 589 nm, and that the evaluation on the sensor response to the glucose solutions requires the use of an optical light source that operates at a central wavelength of 1570 nm. This discrepancy in the frequencies results in dissimilar refractive indices for the same solutions. This fact is owed to the dependence of the refractive index of a material or liquid with the wavelength. To compensate this occurrence, a calibration of the sensor is necessary to estimate the refractive index of the solutions in the optical source wavelength range.

3.1.1.1 Sensor calibration

To perform the sensor calibration, a set of solutions of glycerol with different mass fractions, varying from 0 wt.% to 40 wt.% was prepared, which serve as a reference element. An empirical equation that provides the refractive indices of glycerol solutions at 1550 nm based on their weight percentage has already been reported in the literature, being described as [57]:

$$n(\omega) = -0.0216\omega^3 + 0.0512\omega^2 + 0.111\omega + 1.3165, \tag{3.1}$$

where ω is the mass fraction of the glycerol solutions.

The sensor was then submerged to the glycerol solutions and its spectral response was acquired. The analysis of the MZI consisted on selecting a peak of the high frequency modulation of the spectrum and following the shift it presented with refractive index variations. For the MMI, the bandpass filter was used. Following this process of analysis, one observes by figure 3.3a that the MZI remains unaffected by changes in the refractive index while the MMI component shows a significant variation. Notice that both glucose and glycerol solutions present similar refractive indices in the range considered. Therefore, it is expected that the sensor responds in a similar way. Figure 3.3a shows good agreement on both curves for both solutions of glycerol and glucose. Therefore, based on equation 3.1, a fitting on the sensor tendency would establish the necessary formulation to convert the indices at 1550 nm. Notice that the wavelength shift varies nonlinearly with the concentration of glucose. The equation derived from the glycerol data, $\Delta\lambda(n) = 5872.5825n^2 - 15281.90164n + 9940.76404$ ($r^2 = 0.99827$), can be used to determine the refractive index of the glucose solutions at the operating wavelength. As it is seen from figure 3.3b, a translation for lower values of refractive indices occurs when there is a wavelength increase. The dependence of the refractive indices at both operating wavelengths can be described by a linear fitting of the type $n(\omega) = a\omega + b$,

where a and b are real coefficients, and that are represented on table 3.1. With this, a direct conversion for the refractive indices according to the desired wavelength is settled.

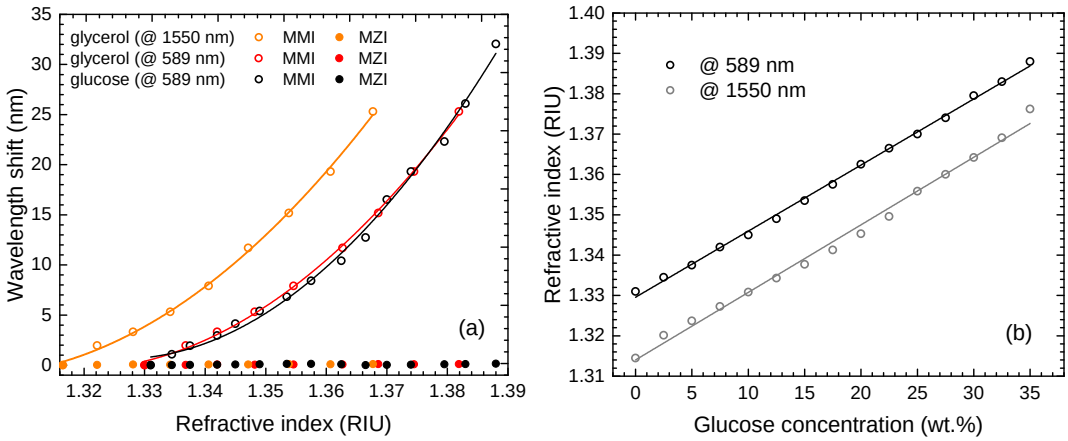

Figure 3.3: (a) Sensor response dependence on refractive index of glycerol and glucose aqueous solutions, for both MZI and MMI, for operating wavelengths of 589 nm and 1550 nm. (b) Refractive index variation with mass fraction for glucose solutions, at 589 nm, and at 1550 nm, where this last was retrieved from the calibration.

Table 3.1: Values of the coefficients attained by the linear fitting at 589 nm and 1550 nm for the glucose solutions.

Operation Wavelength	$n(\omega) = a\omega + b$		
	a	b	r^2
@589 nm	0.00164 ± 0.00002	1.3296 ± 0.0004	0.99809
@1550 nm	0.00167 ± 0.00004	1.3140 ± 0.0008	0.99229

3.1.1.2 Response to refractive index

Once the calibration was carried out, a more thorough discussion about the sensor behaviour can be addressed. In figure 3.4a it is represented the MMI and MZI responses, after calibration, respective to the glucose solutions. As it was already noticed from the previous results, two distinguishable behaviours for the MZI and MMI are perceptible. While the MZI is insensitive to variations on the refractive index, the MMI presents a nonlinear response with a shift towards longer wavelengths (redshift). The insensitivity of the MZI was already expected given that this interferometer occurs within the inner structure of the HSCF. Since variations on the refractive index can only dictate changes on the evanescent field (mediations of the fiber), then, one would anticipate that interferences that occur in the inner fiber structures could not be influenced. On the other hand, mindful that the MMI occurs within the outer cladding, it was predictable that the evanescent field resultant of this interference would be affected by variations of the refractive index. Furthermore, the nonlinear response is also justified since the interference wavelength is highly dependent on the

evanescent field penetration depth, in turn, quadratically correlated with the refractive index of the medium [26]. Given the nonlinear profile of the response, it was necessary to delimit

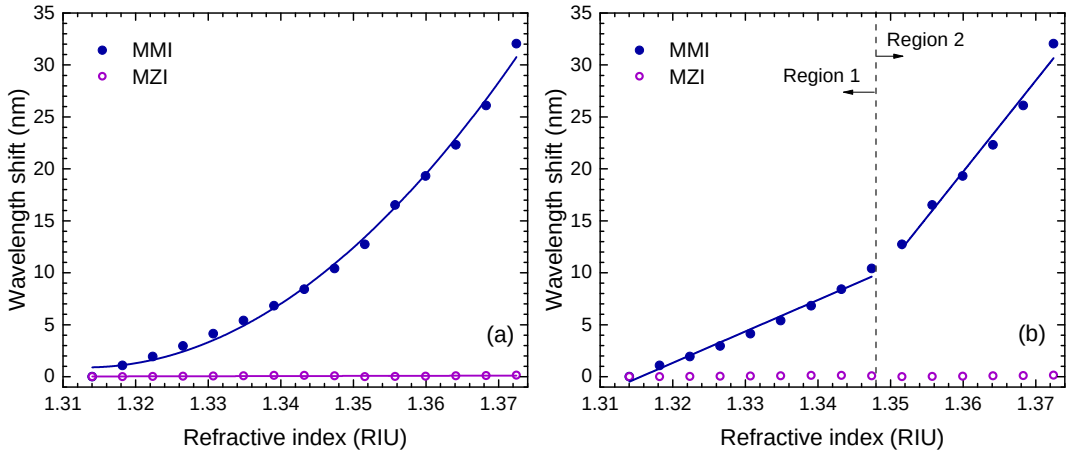

Figure 3.4: (a) Sensor response dependence on the refractive index variation, for both MZI and MMI interferometers. (b) Linearization of the MMI response considering two regions of analysis, namely region 1 [1.310:1.348] RIU and region 2 [1.348:1.381] RIU.

ranges where the response could be approximate to a linear tendency. Hence, two regions were established, a region for the lower refractive indices, designated as region 1 ([1.330:1.348] RIU), and a region for the higher refractive indices, namely region 2 ([1.348:1.381] RIU). In figure 3.4b the linearizations performed for each region are presented. With this, sensitivities of (303 ± 14) nm/RIU ($r^2 = 0.98227$) and (878 ± 60) nm/RIU ($r^2 = 0.97729$) were attained for region 1 and region 2, respectively. On table 3.2 are summarized three examples of MMI sensors, as well as their characteristics, and the HSCF sensor used in this work. From an overall perspective, one might think that the HSCF could not level to other existing MMI sensors in terms of sensitivity. However, the majority of the MMI sensors require an etching

Table 3.2: Table of MMI sensors, including the HSCF sensor used in this work. It is represented the diameter of the fiber, or the multimodal region, the length of the sensors, the range in which they operate and their sensitivities to the refractive index.

Structure device	Diameter	Length	Range	sensitivity	Ref.
SMF-etch MMF-SMF	40 µm	23 mm	1.33-1.3775 RIU	286.2 nm/RIU	[58]
SMF-etch MMF	39 µm	5 mm	1.316-1.353 RIU 1.364-1.397 RIU	338.23 nm/RIU 1012.66 nm/RIU	[26]
SMF-etch MMF-SMF	25 µm	14 mm	1.32-1.35 RIU	1442 nm/RIU	[59]
SMF-HSCF-SMF	**36.5 µm**	**7.5 mm**	**1.31-1.348 RIU** **1.348-1.381 RIU**	**307 nm/RIU** **878 nm/RIU**	**this work**

procedure to enhance their sensitivity. An etching consists of a reduction in the diameter of the fiber, more specifically in the region of the MMI so that the evanescent field may interact more strongly with the external environment. This increases the fragility of the sensor, and sometimes may be highly dangerous since the etching is typically done by resorting to chemi-

cal elements, like the hydrofluoric acid. Therefore, even though in all MMI sensors presented, the diameter of the multimode region is similar, the HSCF sensor stands out from the other in terms of not needing an etching to present sensitivities proximal to the other MMI sensors, making it a sensor that does not need any structural modifications to achieve a high performance. Besides, one denotes the long range of refractive index values that the HSCF sensor can measure. Moreover, the majority of PCFs that are employed in these measurements, often cannot overcome the major problem that still persists in the monitoring of refractive index of liquid media, that lies on the temperature influence. This sensor highlights from the other by being able to discern the temperature, and, therefore, to attain an independent refractive index detection.

3.1.1.3 Evaluation of HSCF length

The response of a 7.50 mm long HSCF sensor was examined and posteriorly compared with other MMI sensors with the objective of evaluating the sensor's length influence on the refractive index sensitivity. Sensors with 3.70 mm, 5.78 mm, 11.00 mm, 11.70 mm, and 16.00 mm were built. As it would be expected, the spectra change considerably as the HSCF length varies. Sensors with higher lengths present a more pronounced MMI component. On the other hand, the smaller the length, the more dominant is the MZI component. This can be noticed in figures 3.5a to 3.5c, where the spectra of the HSCF sensor submerged in water is represented, as well as the bandpass filter, for lengths of 3.70 mm, 7.50 mm and 11.70 mm. The outcome observed complies with what was described in equations 2.10 and 2.12. That is, for smaller values of L, the distance between two adjacent peaks, regarding

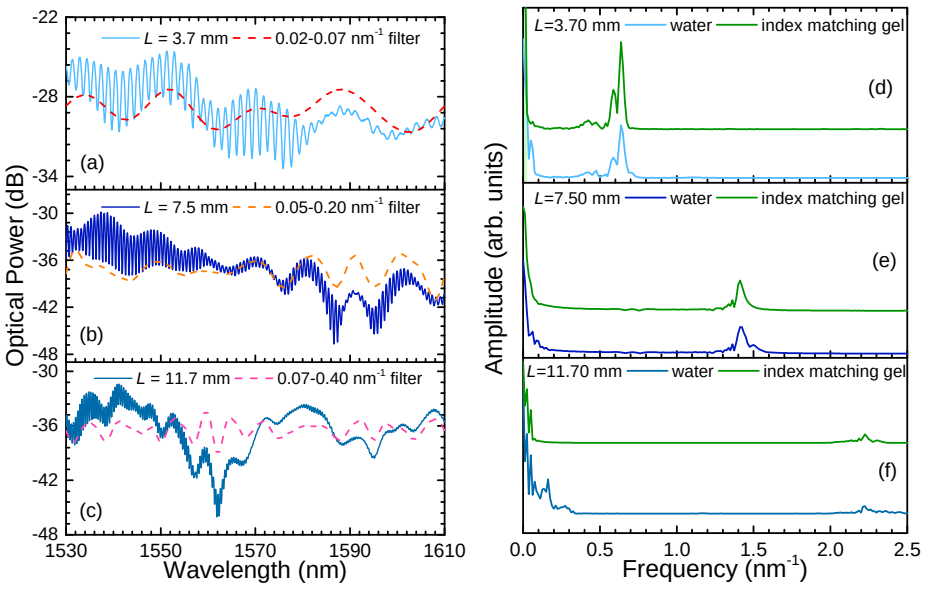

Figure 3.5: (a,b,c) Transmission spectra with the applied filter for three sensors with lengths of 3.70 mm, 7.50 mm and 11.70 mm, respectively, when surrounded by deionized water. (d,e,f) FFT attained for the respective sensors with a surrounding medium of deionized water and index matching gel.

the MZI and MMI components, increases. Although that increase leads to a higher visibility in the spectrum for the MZI component, it results in an overshadow of the MMI, where the spacing between peaks is higher in the spectrum and thus a low perception is attained. The opposite is verified for higher lengths, where the distance between adjacent peaks decreases. Whilst the MMI becomes more distinct, a significant enfeeblement on the MZI happens, since one cannot attain the necessary resolution to view its modulation. This effect is also observed in the frequency domain (figures 3.5d, 3.5e and 3.5f). For comparison purposes, it is also represented the FFT of the spectra of the sensors surrounded by an index matching gel media. This gel has the particularity of presenting a refractive index similar to silica. The FFT of the sensors within this environment show similar behaviour as the water, regarding the MZI component, though, it is clear the disappearance of the MMI component. In fact, the low frequencies disappear since the equality of the refractive index of the gel with silica makes light to see a thicker cladding, translating in a less intense evanescent field. In analogy terms, it resembles an infinite cladding. The described behaviour, that the MMI and MZI present towards different sensor's lengths, can also be appraised by the free spectral range (FSR). The spectral distance between two adjacent peaks ($\lambda_2 - \lambda_1$) was measured for all sensors. The results attained for the MMI and MZI are shown in figures 3.6a and 3.6b, respectively. Notice that the FSR attained for the sensors describe, with good concordance, the tendency

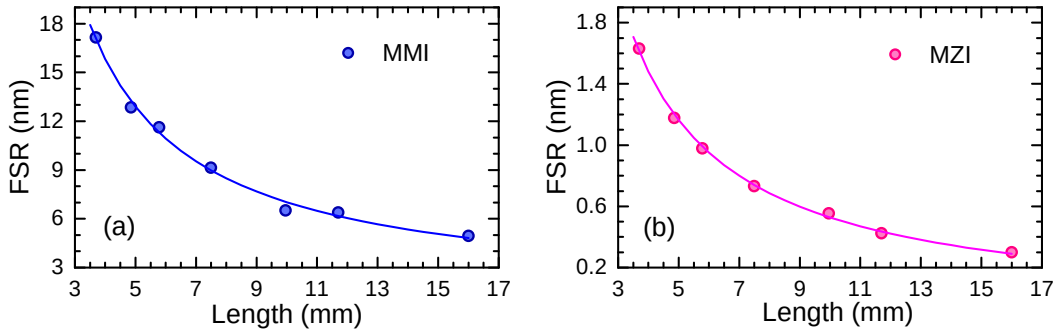

Figure 3.6: FSR dependence on the sensor length for the (a) MMI and (b) MZI.

of equations 2.10 and 2.12 for both MMI and MZI, where one assumed $\lambda_1 \approx \lambda_2$, so that $\lambda_2\lambda_1 = \lambda^2$, with λ being the central wavelength of 1570 nm. Furthermore, the assumption that FSR was small enough to consider that the refractive index was independent of the wavelength, for the frequency range in study, was taken into account. With this simplication, one proceeded to execute a fitting on the FSR curve to an reciprocal function of the type $aL^{-1} + b$, where a and b are real numbers. On table 3.3 are exposed the fitting parameters

Table 3.3: Coefficients and Δn_{eff} attained by the reciprocal fitting for the MZI and MMI.

Sensor	$\text{FSR}(L) = aL^{-1} + b$			
	a (nm^2)	b (nm)	r^2	Δn_{eff}
MMI	$(59 \pm 2) \times 10^6$	1.2 ± 0.3	0.99311	0.042 ± 0.001
MZI	$(64 \pm 1) \times 10^5$	-0.11 ± 0.02	0.99824	0.388 ± 0.007

attained, as well as the difference in the effective refractive indices for both MMI and MZI. For the MMI a value of 0.042 RIU was attained, meaning that the cladding modes that interact with each other have a similar refractive index. As for the MZI, it means that the propagating modes of silica strands with the core modes have a difference in their effective refractive indices of the magnitude of 0.388 RIU.

The later study performed to appraise the influence of the sensor's length consisted on evaluate the sensitivity of the MMI and MZI components. All sensors were characterized to refractive index variations. Towards this objective, a similar experimental procedure to figure 3.1 was conducted for each sensor. In figure 3.7a is represented the responses attained for the different sensors. It is possible to discern that there is a variation on the sensors'

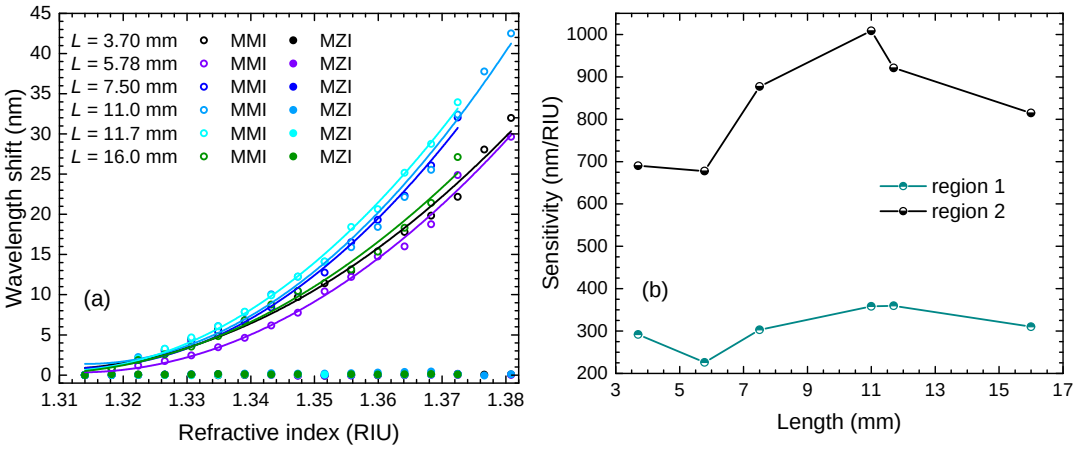

Figure 3.7: (a) Response to the refractive index variation, for both MZI and MMI, of sensors with lengths of 3.70 mm , 5.78 mm, 7.50 mm, 11.00 mm, 11.70 mm and 16.00 mm. (b) Sensitivities attained for the respective sensors in both regions 1 and 2.

response regarding its length. By making the linearizations for the proper regions one attains the sensitivies that are represented in table 3.4. Figure 3.7b illustrates the tendency of the sensitivities with the sensor length, for each region. Given the outcome of the results one cannot establish a direct relation between these two factors. However, it is notorious that there is a propituous length (~ 11 mm) by which the sensor will achieve a maximum sensitivity for both regions, though, further tests should be conducted to improve this analysis.

Table 3.4: Sensitivities attained for the several sensors at both regions.

Sensor Length ±0.02 mm	region 1 [1.310:1.348]		region 2 [1.348:1.381]	
	Sensitivity (nm/RIU)	r^2	Sensitivity (nm/RIU)	r^2
3.70	292 ± 9	0.99314	690 ± 57	0.95347
5.78	226 ± 18	0.95061	678 ± 58	0.9577
7.50	303 ± 14	0.98227	878 ± 60	0.97729
11.00	358 ± 21	0.97398	1008 ± 74	0.96342
11.70	360 ± 20	0.97601	921 ± 45	0.98842
16.00	310 ± 22	0.96181	815 ± 89	0.95426

3.1.1.4 Resolution of the sensor

The performance that an OFS presents is exceedingly important on measuring optical properties where a high reliability is always required. It is often demanded a sensor that can be highly stable and with minimal fluctuations. Therefore, the resolution for refractive index measurements was appraised, using a 9.98 mm long HSCF sensor. The wavelength shift was monitored by making a continuous acquisition of the sensor's transmission spectra over a period of time of 15 minutes for two different solutions. The acquisition rate was approximately 10 seconds. The respective minimum value of refractive index, δn, that this sensor is able to discern is given by [60]:

$$\delta n = \frac{2\sigma_\lambda \Delta n}{\Delta\lambda}, \tag{3.2}$$

where σ_λ is the maximum wavelength standard deviation attained for both solutions, Δn is the variation of the refractive index, and $\Delta\lambda$ the mean wavelength shift. The evaluation of δn was elaborated using solutions of water and 2.5 wt.% glucose, as figure 3.8 shows. For the water sample, a mean wavelength of 1566.97 nm and a standard deviation of 7.1 pm

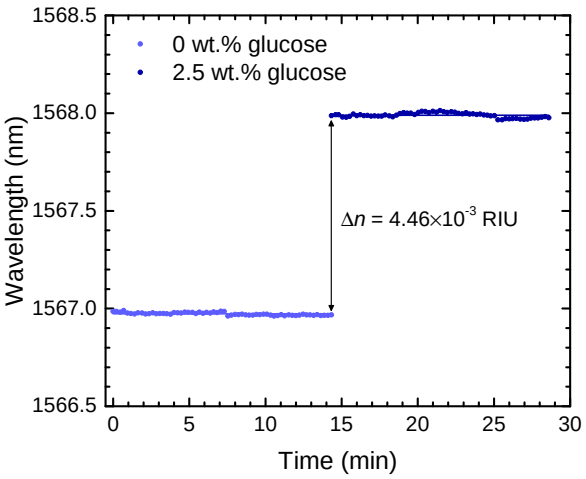

Figure 3.8: Sensor response time to a refractive index step change, using solutions of water and 2.5 wt.% glucose, to evaluate the system resolution.

was determined. For the 2.5 wt.% glucose, the mean wavelength was of 1567.99 nm, with a standard deviation of 12.5 pm. With this, a resolution of 1.09×10^{-4} RIU was attained for the sensing system.

3.1.2 Refractive index and temperature measurements

The monitoring of temperature changes in aqueous environments reveals of extreme importance in many applications. When the temperature of a liquid rises, its refractive index is changed. That variation is quantified by the so-called thermo-optic coefficient (TOC) [61]. As for a solid material, the temperature variation leads to the occurence of two phenomena. There is the thermal expansion, that consists on a variation on the dimensions of the material,

and is quantified by the thermal expansion coefficient (TEC), and there is the thermo-optic effect in the material. Given this, when a OFS is submerged in a temperature varying liquid media, these three effects occur in simultaneous. The thermo-optic and thermal expansion effects, of both liquids and fiber, are often intertwined in the sensor response, which, in many cases, reveals as a challenge to determine and analyse them independently. Therefore, the determination on these components usually requires the use of multiple sensors that can measure them individually, providing a temperature compensation. Due to the existence of two interferometers in the developed sensor, it is possible to use them to measure these parameters, and still establish a temperature compensation.

In order to assess the 7.50 mm long sensor's response to temperature variations within an aqueous environment, a similar setup of figure 3.1 was used, with the difference that the sensor was inserted in a recipient with a liquid volume of approximatly 100 mL. The procedure consisted on pre-heating glucose-water solutions, with concentrations varying between 0 wt.% up to 35 wt.%, using a heating plate. A thermometer was placed near the HSCF to measure the liquid temperature. In this case, both the MMI and MZI present different behaviours to temperature changes, being their responses shown in figure 3.9. It is straightforwardly

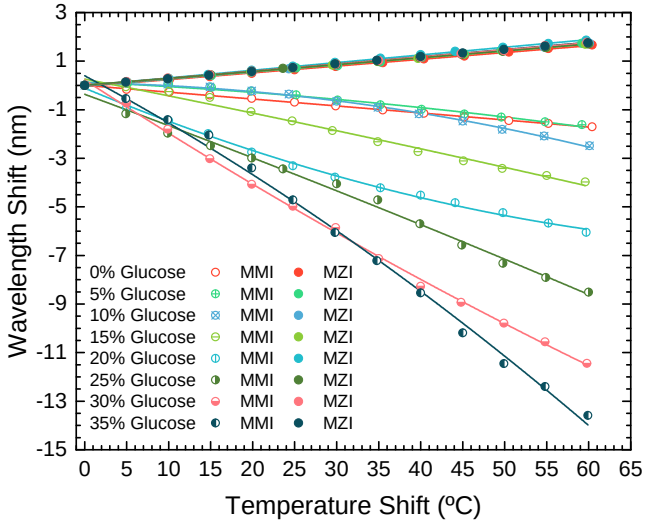

Figure 3.9: HSCF response to temperature shift of the MZI and MMI for the different glucose-water solutions.

observed the linear response of the MZI to temperature variations, with the interference wavelength presenting a redshift, whereas for the MMI one observes the nonlinear response with a blueshift. Notice that the MZI response to temperature regarding the different concentrations of glucose solutions is similar, which allows to conclude that this is only influenced by the thermal expansion and the thermo-optic effect of the silica in the inner strands of the HSCF. In contrast, the MMI response suffers a more accentuated blueshift as the mass fraction of glucose increases, being, therefore, mostly influenced by the changes of the refractive index of the liquid. Assuming that the MMI response will be quadratically dependent on both temperature and refractive index variations, while the MZI only will depend on the

temperature, with a linearly tendency, the wavelength dependence for the MMI and MZI, λ_{MMI} and λ_{MZI}, respectively, can be described as:

$$\lambda_{\mathrm{MMI}}(n,\,T) = \mathrm{K}_{n1}n^2 + \mathrm{K}'_{n1}n + \mathrm{K}''_{n1} + \mathrm{K}_{T1}\,T^2 + \mathrm{K}'_{T1}\,T + \mathrm{K}''_{T1}, \tag{3.3a}$$

$$\lambda_{\mathrm{MZI}}(T) = \mathrm{K}_{T2}\,T + \mathrm{K}'_{T2}, \tag{3.3b}$$

where K_{n1}, K'_{n1} and K''_{n1} are refractive index dependent coefficients, and $\mathrm{K}_{T1,2}$, $\mathrm{K}'_{T1,2}$ and K''_{T1} temperature dependent coefficients attained through the fitting parameters. Given that the MZI response is only affected by temperature changes, then, isolating this parameter in equation 3.3b, and substituting it into equation 3.3a, one attains that the variation in the wavelength caused only by the response to refractive index changes, that is, the temperature compensation wavelenght, λ_{comp}, is given by:

$$\lambda_{\mathrm{comp}}(n) = \lambda_{\mathrm{MMI}} - \mathrm{K}_{T1}\left(\frac{\lambda_{\mathrm{MZI}} - \mathrm{K}'_{T2}}{\mathrm{K}_{T2}}\right)^2 - \mathrm{K}'_{T1}\left(\frac{\lambda_{\mathrm{MZI}} - \mathrm{K}'_{T2}}{\mathrm{K}_{T2}}\right) - \mathrm{K}''_{T1}. \tag{3.4}$$

Equation 3.4 constitutes the solo response of the sensor to changes in the refractive index of the solutions. On the other hand, for practical purposes, it is also important to determine the temperature independent refractive index as a function of concentration. This can be easily accomplished if one uses equation 3.3a, and considers the definition of λ_{comp}, provided in equation 3.4. The final expression is then given by:

$$n_{\mathrm{comp}} = \frac{-\mathrm{K}'_{n1} + \sqrt{\left(\mathrm{K}'_{n1}\right)^2 - 4\mathrm{K}_{n1}.\left(\mathrm{K}''_{n1} - \lambda_{\mathrm{comp}}\right)}}{2\mathrm{K}_{n1}}, \tag{3.5}$$

where the n_{comp} is the temperature independent refractive index. In figures 3.10a and 3.10b are represented the respective response of the MMI without and with the temperature com-

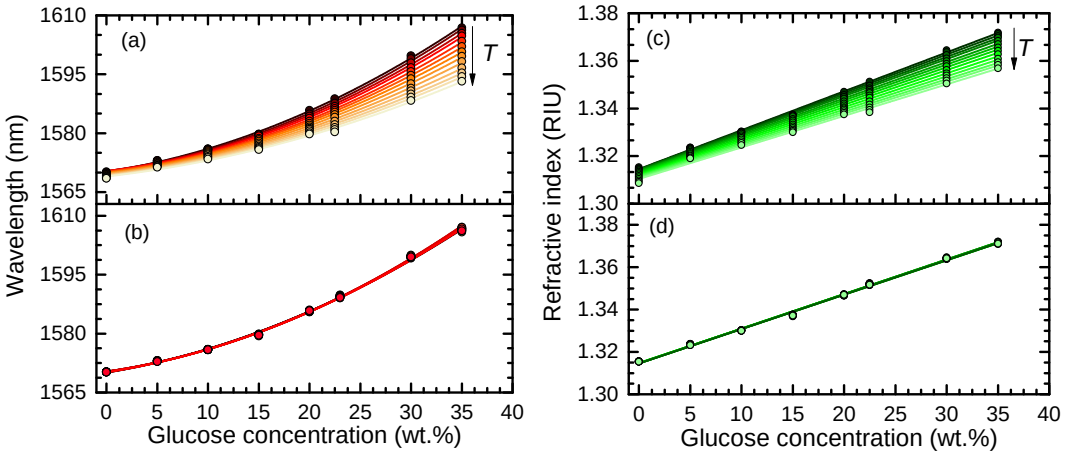

Figure 3.10: Wavelength dependence of glucose concentration (a) without temperature compensation, and (b) with temperature compensation. Refractive index dependence of glucose concentration (c) without temperature compensation, and (d) with temperature compensation.

pensation. Notice that after making the temperature compensation all the curves respective to different temperatures are superimposed, meaning that the wavelength shift is due only to variations on the glucose concentration. Also, figures 3.10c and 3.10d show the refractive index attained before and after the temperature compensation, respectively.

Finally, one proceeded to determine the values of TOC for each solution of glucose. The refractive index change with temperature was appraised for each solution. A linear fitting was stablished for each tendency, being that the slope of the curve would provide the value of the solution's TOC. The attained values are presented in table 3.5. Comparing the TOC of water (0 wt.% of glucose) with the literature [62], where a value of -1.128×10^{-4}RIU/°C was reported, it is possible to infere the good proximity between these. This result evidences the feasibility of this configuration as a temperature independent refractive index sensor.

Table 3.5: TOC values of the studied glucose solutions attained through the linearization of the curves of refractive index variation with temperature.

Glucose concentration (wt.%)	TOC (RIU/°C)	r^2
0	$(-1.13 \pm 0.02) \times 10^{-4}$	0.99647
5	$(-8.4 \pm 0.5) \times 10^{-5}$	0.96401
10	$(-9.7 \pm 0.8) \times 10^{-5}$	0.92664
15	$(-1.39 \pm 0.04) \times 10^{-4}$	0.98822
20	$(-1.55 \pm 0.05) \times 10^{-4}$	0.98532
25	$(-2.08 \pm 0.06) \times 10^{-4}$	0.99038
30	$(-2.38 \pm 0.03) \times 10^{-4}$	0.99839
35	$(-2.63 \pm 0.08) \times 10^{-4}$	0.9881

3.2 Study of ethanol-water mixtures

The role that VOCs play in society is of extreme importance, being their use a recursive one. Its importance is not only dictated by their demand, but also by the danger they may present [32]. A VOC is a compound that is highly unstable at room temperature, and thus, tends to immediatly evaporate [63]. Being ethanol a VOC, then, in some solutions where this element is present (*e.g.*, aqueous ethanol solutions), the ethanol will be the first element to evaporate. The monitoring of the evaporation process has been a matter of deep study by the scientific community. Some of the techniques that are employed nowadays are based on the imaging process, where the analysis of a droplet profile allows to ascertain some properties of the evaporation [64, 65]. An alternative method to this, arises from the use of optical fibers, that not only present a higher resolution, but also allow to infere the variation of some parameters that cannot be achieved by the imaging process. Therefore, different sensing configurations are constantly being developed to achieve an accurate detection as well as monitoring of this type of compounds. Due to this, in this section the characterization of the refractive index of ethanol-water mixtures will be performed, followed by a deep analysis on the evaporation profiles of these solutions.

3.2.1 Refractive index characterization

A set of solutions from the 0 wt.% to the 100 wt.% of ethanol-water mixtures was prepared, with mass fractions varying in 10 wt.%. Those solutions were kept stored for 24 hours to allow their stabilization. Followed by the duly preparation of these, the refractive index respective to each was measured using the Abbe refractometer, and compared with the literature [56], as it is seen from the inset of figure 3.11a. A small shift is still observed between the refractive indices, which may be due to the different room temperature allied with the possibility of a miscalibration on the equipment. Furthermore, it is important to notice that, unlikewise the glucose solutions, the refractive index of the ethanol solutions does not increase linearly with the raise of the mass fraction of ethanol. Instead, it increases nonlinearly until ~ 80 wt.% of ethanol, decreasing afterwards.

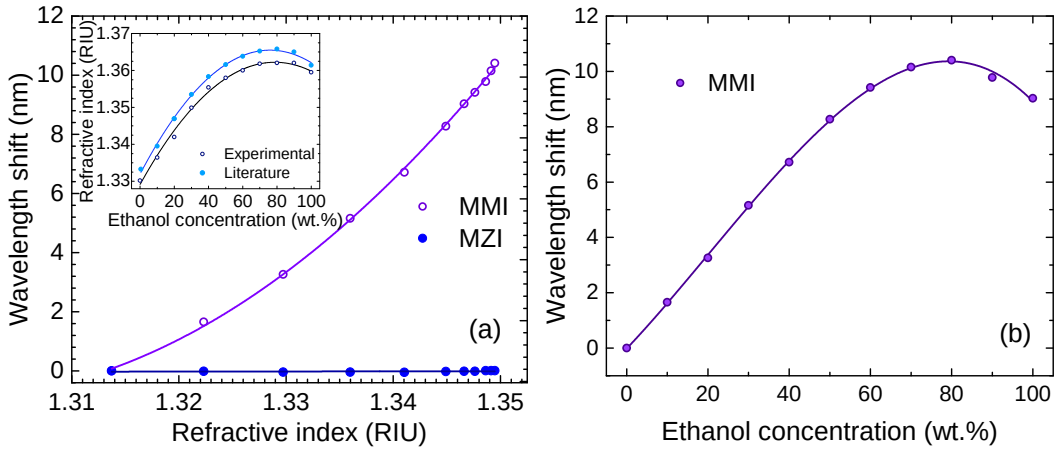

Figure 3.11: (a) Sensor response dependence on the refractive index variation, for the MMI and MZI. Inset: refractive indices for different mass fraction solutions of ethanol-water mixtures measured by the Abbe refractometer, as well as the expected values from the literature [56], at room temperature of 20 °C. (b) Sensor response of the MMI component for ethanol solutions with different concentrations, with the corresponding third order polynomial fit.

Posteriorly, by using a HSCF sensor of 3.70 mm length, and using the same experimental setup as illustrated in figure 3.1, the sensor's response was appraised. Figure 3.11a reveals the responses attained for the MMI and MZI, that, as one would already expect, are similar to the behaviours observed for the glucose solutions. That is, the MMI increases with the increase of the refractive index, and the MZI remains unchanged. By making a linear fitting to the MMI response, a sensitivity of (326 ± 14) nm/RIU ($r^2 = 0.98238$) was attained. In figure 3.11b the sensor response is represented, more specifically the MMI component, to variations on the ethanol concentration, along with a third order polynomial fit:

$$\Delta\lambda_{\mathrm{MMI}} = -1.70218 \times 10^{-5}\omega^3 + 0.00105\omega^2 + 0.15504\omega - 0.01517. \tag{3.6}$$

The established fitting allows to determine the MMI response for any concentration of ethanol, result that will be crucial in the real time monitoring of the evaporation.

3.2.2 Evaporation study

When an aqueous solution starts to evaporate, certain properties of the solution modify, being the refractive index one among them. So, it is possible to study the behaviour of the evaporation process by focusing on changes that occur in real time to this parameter. In virtue of this, it was explored the use of the HSCF in detecting these changes, hence, monitoring the evaporation.

Figure 3.12 displays the experimental setup used to monitor the evaporation, where two different substrates, teflon and glass, were used. The sensor was placed on top of the substrate

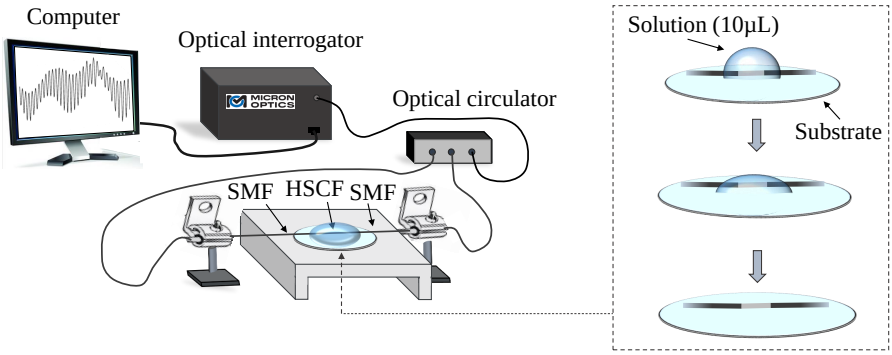

Figure 3.12: Scheme of the experimental setup used on the evaporation process.

and a 10 µL droplet of the solution was placed above the sensing head, with a micropipette. Only the solutions 0 wt.%, 20 wt.%, 50 wt.%, 70 wt.% and 100 wt.%, were used to study the evaporation. The experimental procedure consisted on acquiring the spectral response of the sensor, with an acquisition rate of 10 seconds, using the optical interrogator (Micron Optics SM125) with a resolution of 0.005 nm, till the droplet was completly evaporated. The setup was implemented in a transmission configuration, where the optical interrogator served the dual purpose of an optical light source and a spectrum analyzer, with the help of an optical circulator that redirects the light that comes from the interrogator to the sensor, and returns it, afterwards, to the optical interrogator.

The monitoring of the evaporation process was carried out by analyzing the MMI, due to its sensitivity to variations in the external medium. With this, to monitor the MMI response, a 0.1 nm^{-1} low pass filter was applied to the acquired spectra, and the wavelength shift of a peak was monitored. The wavelength shift of the MMI attained for the studied solutions, using a glass substract and teflon substract, are respectively presented in figures 3.13a and 3.13b. In the evaporation profiles, different stages of evaporation can be identified, according to the concentration of ethanol. For instance, during the evaporation of water (0 wt.%), the refractive index of the solution remains unaltered, leading to a constant response by the MMI. Only when there is a transition between the liquid medium and the air, an abrupt decrease on the wavelength is verified, that corresponds to the high difference between the refractive indices of water and the air that the sensor detects. As for the solutions that contain a percentage of ethanol, namely the 20 wt.%, 50 wt.% and 70 wt.%, a different

response is exhibited. In a first stage, a decrease in the wavelength is verified due to the decrease in the refractive index, which corresponds to the evaporation of the ethanol. After

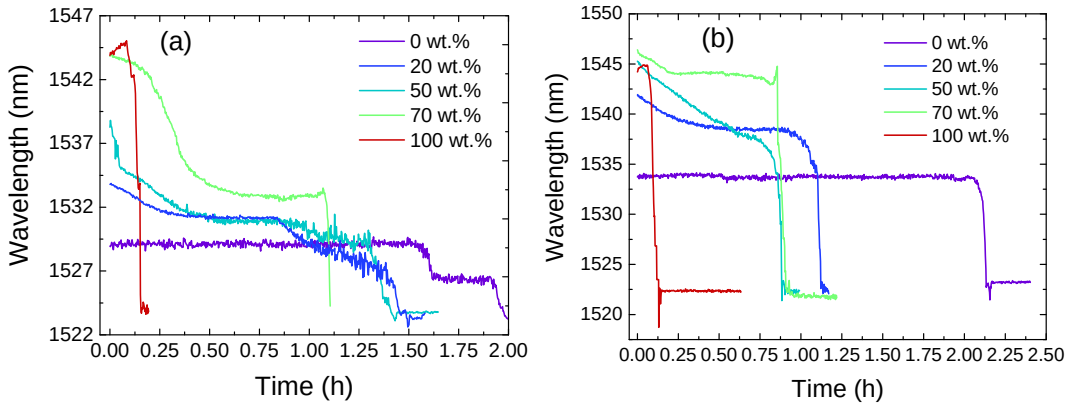

Figure 3.13: Evaporation profiles for ethanol-water mixtures with different concentrations of ethanol, using a substrate of (a) glass and (b) teflon.

its evaporation, the remaining solution will be mainly composed by water, meaning that it will not cause major variations in the refractive index of the solution. It is, then, verified a constant response by the MMI during this stage. Similarly to the water sample, in the 100 wt.% of ethanol, one might expect that a evaporation of a unique element would not lead to a change in the refractive index during its evaporation. However, it is initially observed a slight increase in the wavelength, meaning that there was a slim increase in the refractive index. This can be justified by the absorption of water molecules from the ethanol, derived from its hygroscopicity [66]. Furthermore, notice that the high instability of ethanol, allied with the small volume of solution, leads to a fast evaporation when compared with the other solutions. The described behavior for each solution is verified in both substrates.

In an overall perspective the evaporation profiles attained for both substrates are similar, though some discrepancies are noticed, specially in the 70 wt.%. This may be possibly originated by the influence of external factors, such as the variation of the room temperature and the applied strain in the HSCF sensor, in the preparation of the experimental setup, for each solution. Notice that after the evaporation experiment, the sensor was removed and cleaned. Therefore the conditions in which both measurements were done may have experienced different conditions.

Moreover, it is important to notice the difference in the evaporation time for both substrates, where for the teflon substrate the evaporation process was longer. The subject of evaporation in substrates, that present dissimilar surface properties, is a matter of great discussion. There are several factors that one can address to justify the observed differences in these, among them, the dissimilar evaporation dynamics, and the different surface tensions and flow motions [65]. When a teflon substrate is used, a spherical cap-shaped droplet is attained, whilst in a glass substrate the droplet spreads over, loosing its concentrical shape, as the ethanol concentration increases. In other words, the surface area of the droplet is higher in the glass substrate than the teflon substrate, and tends to increase as the ethanol

concentration also increases. Still, this is a complex topic that would require further studies.

The final part of the evaporation study consisted on converting the acquired spectral responses to variations of ethanol concentration. The relation between the MMI response with the concentration of ethanol, that is expressed by equation 3.6, was used. Making the conversion it was possible to attain the real time variation of the ethanol concentration for each solution, as figures 3.14a and 3.14b depict. This result is important in many applications where a fast monitoring is required. It is possible, then, to monitor the concentration of ethanol in a liquid medium, using a small and robust optical device.

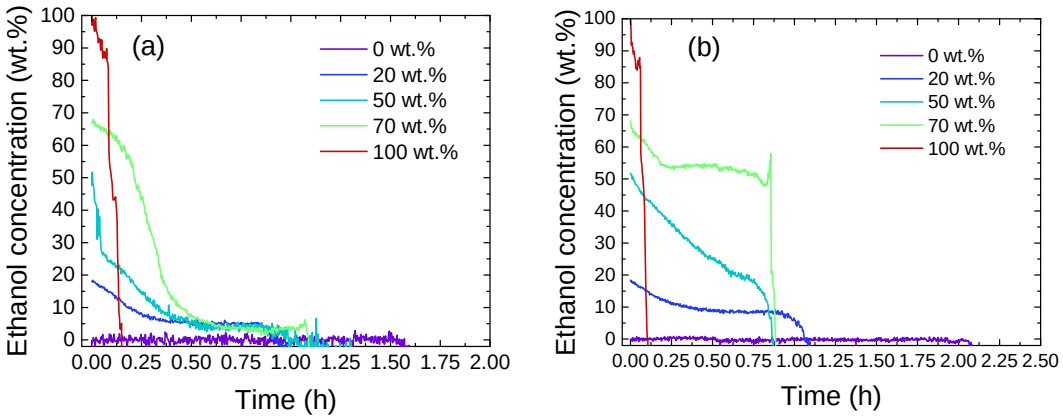

Figure 3.14: Temporal profile of the ethanol concentration for (a) glass substrate and (b) teflon substrate.

4. Characterization in air media

The purpose of this study relies on observing and evaluating how each interferometer component responds when subjected to physical parameters, and to evaluate the future prospect of usage of the sensor in measuring simultaneous parameters. To extend the study to all components of the sensor, namely, the MMI, MZI, IR and ER, two different broadbands were used. In the first broadband, the C+L bands (1530 nm-1610 nm), a study to the MMI, MZI and ER responses to the curvature, temperature and strain was performed. In the second broadband (900 nm-1300 nm), the response of the IR and ER to curvature and temperature was evaluated.

4.1 Evaluation of physical parameters: 1530 nm - 1610 nm

4.1.1 Response to temperature

The temperature measurements were conducted by using the experimental setup depicted in figure 4.1, where the typical transmission apparatus was established. Also, a Peltier cooler and a temperature controller were used to induce temperature variations in the sensor's surroundings. A 9.98 mm length HSCF was used as sensing head. The experimental procedure consisted on varying the temperature from the 20 °C to 85 °C, in steps of 5 °C, and to collect the sensor spectral response. In figure 4.2a is depicted the spectral response of the sensor

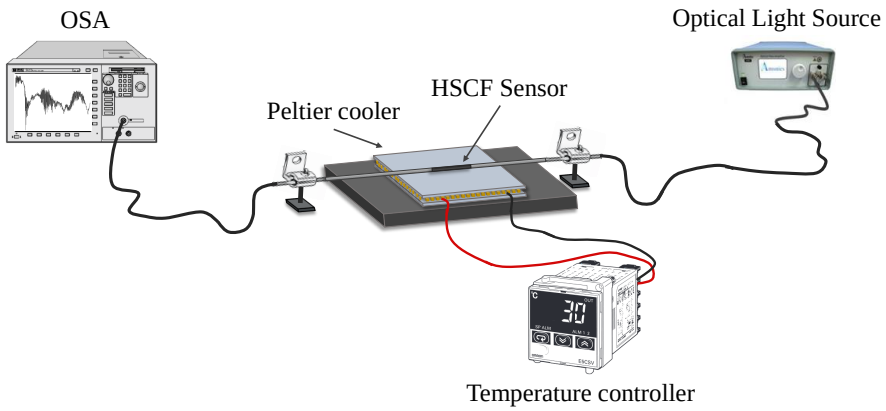

Figure 4.1: Experimental setup used for the temperature measurements.

under normal conditions, at room temperature. From the observation of the spectrum it is also possible to ascertain the existance of a high frequency domain being modulated by a low frequency, where the high frequency results from the MZI and the low frequency from both the MMI and the ER. Notice that this study is being carried out in the C+L bands, therefore there are no resonance wavelengths resultant from the IR. With this, the wavelength shift

of the MZI component was attained by directly resorting to the transmission spectrum, and the wavelength shift of the MMI and ER components were attained by performing a 0.1 – 0.2 nm^{-1} band pass filter to the transmission spectrum, as figure 4.2b indicates. The attained

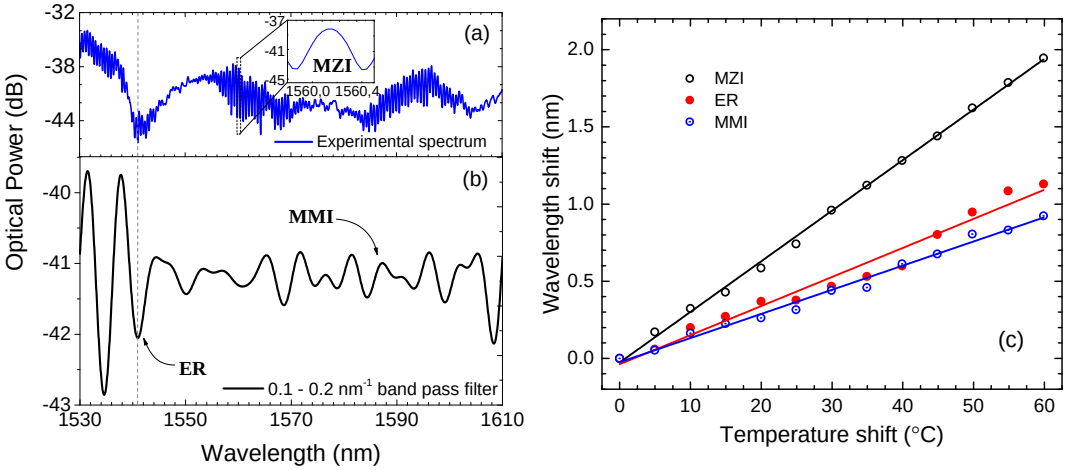

Figure 4.2: (a) Spectral response of the HSCF, with an inset showing the MZI peak that was monitored. (b) Curve attained by applying a 0.1-0.2 nm^{-1} band pass filter used to monitor the external AR dip and the MMI peak. (c) Wavelength shift dependence with temperature, of the MZI, ER and MMI components.

results are represented in figure 4.2c, where a linear tendency is verified in all components, as well as a shift towards longer wavelengths (red shift). A linear fitting was carried out at the acquired data, achieving a temperature sensitivity of $(32.8 \pm 0.4)\,\mathrm{pm/°C}$ ($r^2 = 0.998$) for the MZI, a sensitivity of $(19 \pm 1)\,\mathrm{pm/°C}$ ($r^2 = 0.96852$) for the ER and $(15.7 \pm 0.5)\,\mathrm{pm/°C}$ ($r^2 = 0.98771$) for the MMI. The expected temperature sensitivities for each component, can be derived from the temperature dependence applied to equations 2.11, 2.3, and 2.9, respectively, which result in:

$$\begin{aligned}\frac{\partial \lambda_{\mathrm{MZI}}}{\partial T} &= \frac{n_{\mathrm{eff}}^{\mathrm{Si}} - n_{\mathrm{eff}}^{\mathrm{a}}}{p}\frac{\partial L}{\partial T} + \frac{L}{p}\frac{\partial n_{\mathrm{eff}}^{\mathrm{Si}}}{\partial T} \\ &= \left(\frac{1}{L}\frac{\partial L}{\partial T} + \frac{n_{\mathrm{eff}}^{\mathrm{Si}}}{n_{\mathrm{eff}}^{\mathrm{Si}} - n_{\mathrm{eff}}^{\mathrm{a}}}\frac{1}{n_{\mathrm{eff}}^{\mathrm{Si}}}\frac{\partial n_{\mathrm{eff}}^{\mathrm{Si}}}{\partial T}\right)\lambda_{\mathrm{MZI}} = \left(\alpha + \frac{n_{\mathrm{eff}}^{\mathrm{Si}}}{n_{\mathrm{eff}}^{\mathrm{Si}} - n_{\mathrm{eff}}^{\mathrm{a}}}\beta\right)\lambda_{\mathrm{MZI}}\,,\end{aligned} \tag{4.1}$$

$$\begin{aligned}\frac{\partial \lambda_m}{\partial T} &= \frac{2\sqrt{n_{\mathrm{Si}}^2 - n_{\mathrm{a}}^2}}{m}\frac{\partial w}{\partial T} + \frac{2 n_{\mathrm{Si}} w}{m\sqrt{n_{\mathrm{Si}}^2 - n_{\mathrm{a}}^2}}\frac{\partial n_{\mathrm{Si}}}{\partial T} \\ &= \left(\frac{1}{w}\frac{\partial w}{\partial T} + \frac{n_{\mathrm{Si}}^2}{n_{\mathrm{Si}}^2 - n_{\mathrm{a}}^2}\frac{1}{n_{\mathrm{Si}}}\frac{\partial n_{\mathrm{Si}}}{\partial T}\right)\lambda_m = \left(\alpha + \frac{n_{\mathrm{Si}}^2}{n_{\mathrm{Si}}^2 - n_{\mathrm{a}}^2}\beta\right)\lambda_m\,,\end{aligned} \tag{4.2}$$

$$\frac{\partial \lambda_{\mathrm{MMI}}}{\partial T} = \frac{n_{\mathrm{eff}}^{\mathrm{cl}_i} - n_{\mathrm{eff}}^{\mathrm{cl}_j}}{p}\frac{\partial L}{\partial T} + \frac{L}{p}\left(\frac{\partial n_{\mathrm{eff}}^{\mathrm{cl}_i}}{\partial T} - \frac{\partial n_{\mathrm{eff}}^{\mathrm{cl}_j}}{\partial T}\right)$$
$$= \left(\frac{1}{L}\frac{\partial L}{\partial T} + \frac{1}{n_{\mathrm{eff}}^{\mathrm{cl}_i} - n_{\mathrm{eff}}^{\mathrm{cl}_j}}\left(\frac{\partial n_{\mathrm{eff}}^{\mathrm{cl}_i}}{\partial T} - \frac{\partial n_{\mathrm{eff}}^{\mathrm{cl}_j}}{\partial T}\right)\right)\lambda_{\mathrm{MMI}}, \tag{4.3}$$

where $\alpha = 5.5 \times 10^{-7}\,^{\circ}\mathrm{C}^{-1}$ and $\beta = 8.6 \times 10^{-6}\,^{\circ}\mathrm{C}^{-1}$ [11] are the silica's TEC and TOC, respectively. Note that p is the wavelength order of constructive interference, regarding the MZI and MMI, and m the resonance order (destructive interference) of the AR guidance. Also, notice that in the derivation of the wavelength shift of the ER with temperature it was considered that $\theta \approx 90°$, and that its variation with temperature was minimal. With this, it is possible to predict the sensitivity for each component. It was considered $\lambda_{\mathrm{MZI}} \approx 1560\,\mathrm{nm}$, $\lambda_m \approx 1540\,\mathrm{nm}$, and a first approximation of $n_{\mathrm{eff}}^{\mathrm{Si}} = n_{\mathrm{Si}} = 1.444$ was established. Values of $\sim 44.5\,\mathrm{pm/°C}$ and $\sim 26.3\,\mathrm{pm/°C}$ were respectively obtained for the MZI and ER, being these quite proximate to the experimental ones. The slight difference may be due to the approximations that were considered. Notice that the thermo-optic effect is dominant over the thermal expansion, meaning that a small variation in this coefficient may lead to a considerable change in the expected sensitivity. The temperature dependence of the MMI is more complicated to estimate since the modes interact within the silica material and may experience different conditions. Therefore, one can only conclude that in the MMI the thermo-optic effect will have a lower impact in the spectral response when compared to the MZI and ER, as it is indeed experimentally observed.

4.1.2 Response to curvature

The curvature measurements were carried out using the experimental apparatus depicted in figure 4.3. The sensor was displaced between a fixed stage and a translation stage, where

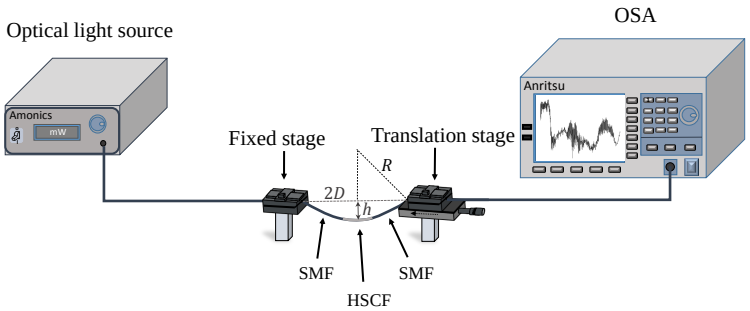

Figure 4.3: Experimental setup used on the curvature measurements.

the movement of this last, towards the direction of the fixed stage, would induce a bending on the sensor. The curvature (C) that the sensor is subjected to can be determined by the

expression:

$$C = R^{-1} = \frac{2h}{h^2 + D^2}, \tag{4.4}$$

where $2D$ is 32.3 cm, and corresponds to the distance between points where the sensor is fixed, h is the height of the sensor center in relation to the horizontal plane, and R is the radius of sensor bending. In the curvature measurements, the sensor was bended to a maximum height (h) of 15 mm, which corresponds to a curvature of approximately 1.51 m^{-1}, in steps of 1 mm. In figure 4.4a are represented the attained experimental results. It is perceptible not only the

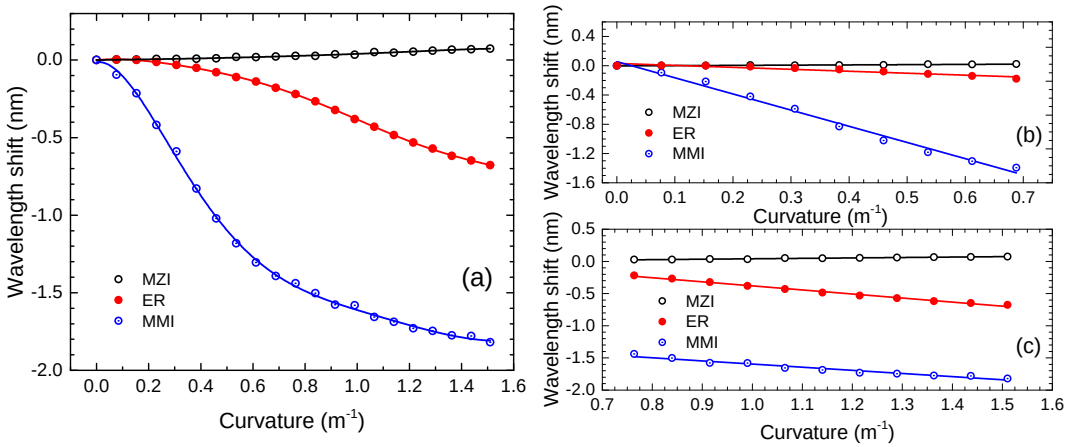

Figure 4.4: (a) Wavelength shift dependence with curvature, of the MZI, ER and MMI components. The fittings were applied for easiness of perception. (b) Responses attained for each component to curvature in the first domain, that ranges from 0 m^{-1} to 0.7 m^{-1}. (c) Responses attained for each component to curvature in the second domain, that ranges from 0.7 m^{-1} to 1.51 m^{-1}.

opposite responses of the MZI (redshift) in relation to the MMI and ER (blueshift), but also the nonlinear behaviour towards the curvature, which is more accentuated in the later. Facing this, it was necessary to analyse the responses in two different curvature domains, where the response can be considered as linear, as figures 4.4b and 4.4c show. In table 4.1 are presented the attained sensitivities for the MZI, ER and MMI, for both curvature ranges. In the first

Table 4.1: Sensitivities attained for the MZI, ER, and MMI at both curvature domains.

Curvature range	MZI		ER		MMI	
	Sens. (nm/m^{-1})	r^2	Sens. (nm/m^{-1})	r^2	Sens. (nm/m^{-1})	r^2
0 m^{-1} - 0.70 m^{-1}	0.033 ± 0.004	0.90842	-0.27 ± 0.03	0.90691	-2.21 ± 0.08	0.98881
0.70 m^{-1} - 1.51 m^{-1}	0.067 ± 0.004	0.96148	-0.63 ± 0.02	0.99202	-0.49 ± 0.03	0.9535

domain, the MMI was the component that revealed the highest sensitivity, whereas in the second curvature domain it was the ER.When the fiber is bended, two different phenomena may occur, as shown in figure 4.5. Firstly, in the bending process, a side of the fiber is stretched while the other is compressed. However there is a neutral bending plane (neutral axis), where no strain is applied. Due to the elasto-optic property of materials, the application

of a strain leads to a change in the refractive index of the material [67], and thus, different responses by the HSCF components. The negligible sensitivity by the MZI may be explained

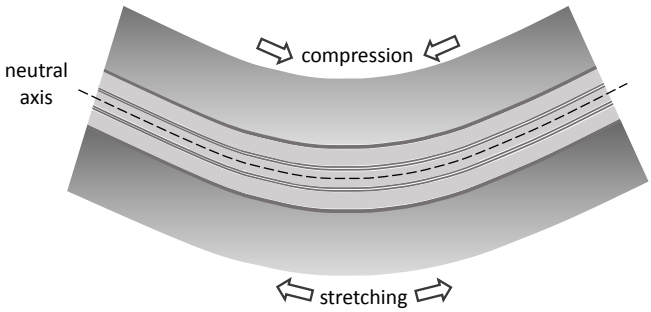

Figure 4.5: Scheme of he HSCF bended. The dash line represents the neutral axis of the fiber.

by the proximity of its location to the neutral axis, where there is no significant variation in the refractive index. In contrary the ER and MMI depend strongly on this variation. Moreover, a variation in the incident angle of light can also contribute to the verified responses. Further studies could be performed using a finite elements-based software (*e.g.* Solidworks), to verify the validity of these assumptions.

4.1.3 Response to strain

The strain measurements were conducted by resorting to a experimental setup similar to the figure 4.3. The sensor was fixed at both ends to a non-movable stage and to a translation stage, where $2D$ was 29.7 cm. However, in this case the movement of the translation stage was done in the opposite direction of the non-movable stage. The strain measurement was carried out by stretching the fiber to a total elongation of 0.18 mm, in steps of 0.02 mm, corresponding to a maximum strain of $\sim$ 600 µε. The experimental results attained are represented in figure 4.6. All components exhibited linear tendencies, however, the ER and

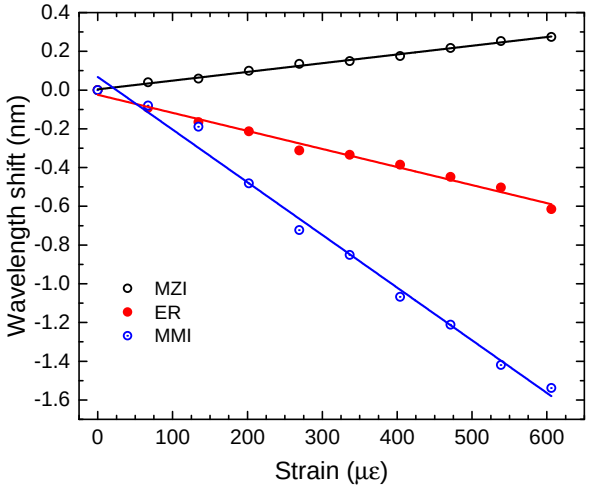

Figure 4.6: Wavelength shift dependence with strain, of the MZI, ER and MMI.

the MMI presented blueshift response, while the MZI presented a redshift response. It was obtained a sensitivity of $(0.45 \pm 0.01)\,\mathrm{pm/\mu\varepsilon}$ ($r^2 = 0.99451$) for the MZI, a sensitivity of $(-0.93 \pm 0.04)\,\mathrm{pm/\mu\varepsilon}$ ($r^2 = 0.98658$) for the ER, and a sensitivity of $(-2.72 \pm 0.09)\,\mathrm{pm/\mu\varepsilon}$ ($r^2 = 0.99006$) for the MMI. Following the same process as in the temperature analysis, a prediction of the strain sensitivities can be established by determining the strain dependence. For the MZI the following relationship is attained:

$$\begin{aligned}\frac{\partial\lambda_{\mathrm{MZI}}}{\partial\varepsilon} &= \frac{n_{\mathrm{eff}}^{\mathrm{Si}} - n_{\mathrm{eff}}^{\mathrm{a}}}{p}\frac{\partial L}{\partial\varepsilon} + \frac{L}{p}\frac{\partial n_{\mathrm{eff}}^{\mathrm{Si}}}{\partial\varepsilon} \\ &= \left(\frac{1}{L}\frac{\partial L}{\partial\varepsilon} + \frac{n_{\mathrm{eff}}^{\mathrm{Si}}}{n_{\mathrm{eff}}^{\mathrm{Si}} - n_{\mathrm{eff}}^{\mathrm{a}}}\frac{1}{n_{\mathrm{eff}}^{\mathrm{Si}}}\frac{\partial n_{\mathrm{eff}}^{\mathrm{Si}}}{\partial\varepsilon}\right)\lambda_{\mathrm{MZI}} = \left(1 - \frac{n_{\mathrm{eff}}^{\mathrm{Si}}}{n_{\mathrm{eff}}^{\mathrm{Si}} - n_{\mathrm{eff}}^{\mathrm{a}}}\rho_\varepsilon\right)\lambda_{\mathrm{MZI}}\,,\end{aligned} \tag{4.5}$$

where ρ_ε is the effective photoelastic coefficient, and is given by [11, 68]:

$$\rho_\varepsilon = -\frac{1}{n_{\mathrm{eff}}^{\mathrm{Si}}}\frac{\partial n_{\mathrm{eff}}^{\mathrm{Si}}}{\partial\varepsilon} = \frac{(n_{\mathrm{eff}}^{\mathrm{Si}})^2}{2}\left(\rho_{12} - \upsilon(\rho_{11} + \rho_{12})\right), \tag{4.6}$$

with $\rho_{11} = 0.121$ and $\rho_{12} = 0.27$ [56] the components of the strain-optic tensor (Pockel's coefficients) and $\upsilon = 0.17$ [69] the Poisson ratio, for fused silica. Furthermore, $\partial\varepsilon = \partial L/L$. For the ER and MMI the sensitivities can be expressed by:

$$\begin{aligned}\frac{\partial\lambda_m}{\partial\varepsilon} &= \frac{2\sqrt{n_{\mathrm{Si}}^2 - n_{\mathrm{a}}^2}}{m}\frac{\partial w}{\partial\varepsilon} + \frac{2wn_{\mathrm{Si}}}{m\sqrt{n_{\mathrm{Si}}^2 - n_{\mathrm{a}}^2}}\frac{\partial n_{\mathrm{Si}}}{\partial\varepsilon} \\ &= \left(\frac{1}{w}\frac{\partial w}{\partial\varepsilon} + \frac{n_{\mathrm{Si}}^2}{n_{\mathrm{Si}}^2 - n_{\mathrm{a}}^2}\frac{1}{n_{\mathrm{Si}}}\frac{\partial n_{\mathrm{Si}}}{\partial\varepsilon}\right)\lambda_m = \left(-\upsilon + \frac{n_{\mathrm{Si}}^2}{n_{\mathrm{Si}}^2 - n_{\mathrm{a}}^2}\rho_\varepsilon\right)\lambda_m\,,\end{aligned} \tag{4.7}$$

$$\begin{aligned}\frac{\partial\lambda_{\mathrm{MMI}}}{\partial\varepsilon} &= \frac{n_{\mathrm{eff}}^{\mathrm{cl}_i} - n_{\mathrm{eff}}^{\mathrm{cl}_j}}{p}\frac{\partial L}{\partial\varepsilon} + \frac{L}{p}\frac{\partial n_{\mathrm{eff}}^{\mathrm{cl}_i}}{\partial\varepsilon} - \frac{L}{p}\frac{\partial n_{\mathrm{eff}}^{\mathrm{cl}_j}}{\partial\varepsilon} \\ &= \left(\frac{1}{L}\frac{\partial L}{\partial\varepsilon} + \frac{n_{\mathrm{eff}}^{\mathrm{cl}_i}}{n_{\mathrm{eff}}^{\mathrm{cl}_i} - n_{\mathrm{eff}}^{\mathrm{cl}_j}}\frac{1}{n_{\mathrm{eff}}^{\mathrm{cl}_i}}\frac{\partial n_{\mathrm{eff}}^{\mathrm{cl}_i}}{\partial\varepsilon} - \frac{n_{\mathrm{eff}}^{\mathrm{cl}_j}}{n_{\mathrm{eff}}^{\mathrm{cl}_i} - n_{\mathrm{eff}}^{\mathrm{cl}_j}}\frac{1}{n_{\mathrm{eff}}^{\mathrm{cl}_j}}\frac{\partial n_{\mathrm{eff}}^{\mathrm{cl}_j}}{\partial\varepsilon}\right)\lambda_{\mathrm{MMI}} \\ &= \left(1 - \frac{n_{\mathrm{eff}}^{\mathrm{cl}_j}}{n_{\mathrm{eff}}^{\mathrm{cl}_i} - n_{\mathrm{eff}}^{\mathrm{cl}_j}}\rho_\varepsilon^i + \frac{n_{\mathrm{eff}}^{\mathrm{cl}_j}}{n_{\mathrm{eff}}^{\mathrm{cl}_i} - n_{\mathrm{eff}}^{\mathrm{cl}_j}}\rho_\varepsilon^j\right)\lambda_{\mathrm{MMI}}\,,\end{aligned} \tag{4.8}$$

where ρ_ε^i and ρ_ε^j are the photoelastic coefficients of silica that the modes i and j experience. Moreover, notice that $\partial w/w = -\upsilon\partial\varepsilon$. With this, and again considering that the incident angle variation in the AR guidance is not dominant, then, through equations 4.5 and 4.7, sensitivities of $\sim 0.48\,\mathrm{pm/\mu\varepsilon}$ and $\sim -0.89\,\mathrm{pm/\mu\varepsilon}$ were calculated for the MZI and ER, respectively, revealing similar to the ones experimentally acquired. Once more, the analysis to the MMI is more challenging, though, according to the experimental results, it is perceptible that the second term of equation 4.8 is the dominant one. Still, the attained sensitivity is within the values found in the literature for optical fiber sensors based on MMI [14, 70].

4.1.4 Simultaneous measurement of temperature, curvature and strain

The results achieved reveal the practicability of the sensor in performing simultaneous measurements of the studied parameters. The distinct responses that the intrinsic components of the sensor presented to each measurand, *i.e.*, strain ($\Delta\varepsilon$), curvature (ΔC), and temperature (ΔT), can be described by the following matricial relation:

$$\begin{pmatrix} \Delta\lambda_{\mathrm{MZI}} \\ \Delta\lambda_{\mathrm{ER}} \\ \Delta\lambda_{\mathrm{MMI}} \end{pmatrix} = \begin{pmatrix} K_{\varepsilon,\mathrm{MZI}} & K_{C,\mathrm{MZI}} & K_{T,\mathrm{MZI}} \\ K_{\varepsilon,\mathrm{ER}} & K_{C,\mathrm{ER}} & K_{T,\mathrm{ER}} \\ K_{\varepsilon,\mathrm{MMI}} & K_{C,\mathrm{MMI}} & K_{T,\mathrm{MMI}} \end{pmatrix} \begin{pmatrix} \Delta\varepsilon \\ \Delta C \\ \Delta T \end{pmatrix}, \tag{4.9}$$

where the variable $K_{i,j}$ stands for the sensitivity of the studied parameter i, of the corresponding sensing component j. Substituting the sensitivities with the respective values, it is obtained:

$$\begin{pmatrix} \Delta\lambda_{\mathrm{MZI}} \\ \Delta\lambda_{\mathrm{ER}} \\ \Delta\lambda_{\mathrm{MMI}} \end{pmatrix} = \begin{pmatrix} 0.45 & 33 & 32.8 \\ -0.93 & -270 & 18.9 \\ -2.72 & -2210 & 15.7 \end{pmatrix} \begin{pmatrix} \Delta\varepsilon \\ \Delta C \\ \Delta T \end{pmatrix}. \tag{4.10}$$

By proceeding to an inversion of the matrix, it is possible to acquire the direct variation of the parameters according to spectral fluctuations on the sensor:

$$\begin{pmatrix} \Delta\varepsilon \\ \Delta C \\ \Delta T \end{pmatrix} = \begin{pmatrix} 0.6361 & -1.2374 & 0.16067 \\ -0.00062 & 0.00163 & -0.00066 \\ 0.02238 & 0.01533 & -0.00153 \end{pmatrix} \begin{pmatrix} \Delta\lambda_{\mathrm{MZI}} \\ \Delta\lambda_{\mathrm{ER}} \\ \Delta\lambda_{\mathrm{MMI}} \end{pmatrix}. \tag{4.11}$$

Note that the units of $\Delta\varepsilon$, ΔC, ΔT, and $\Delta\lambda_{\mathrm{MZI,ER,MMI}}$, are $\mu\varepsilon$, m^{-1}, °C, and pm, respectively.

4.2 Evaluation of physical parameters: 900 nm - 1300 nm

4.2.1 Response to curvature

The curvature measurements were carried out using a sensing head of 7.2 mm, that was displaced in a similar setup as depicted in figure 4.3, though instead of an optical light source operating in the C+L band, a supercontinuum light source (LEUKOS SAMBA 450) was used. Furthermore, a resolution of 0.2 nm was set in the OSA. The distance between the stages ($2D$), was 27.5 cm, and the sensor was bended to a maximum height of 20 mm, corresponding to a maximum curvature of approximately $1.87\,\mathrm{m}^{-1}$. The decrease of height was done in steps of 2 mm. In figure 4.7a is depicted the sensor spectrum in the visible and infrared windows, with no curvature applied, and in figure 4.7b the frequency window that was monitored. Notice that to reduce the associated noise to the spectrum, and to obtain a more perceptible view of the ER dips, a $0.11\,\mathrm{nm}^{-1}$ low pass filter was applied. To monitor the IR dip, a gaussian fit was applied to the entire depression band, whereas for the ER the λ_{62} was monitored. The experimental results attained for the IR and ER are presented in figure 4.7c, where it is notorious that both components shift towards smaller wavelengths (blue

shift). Additionally, from the results one can infere that both resonance responses presented

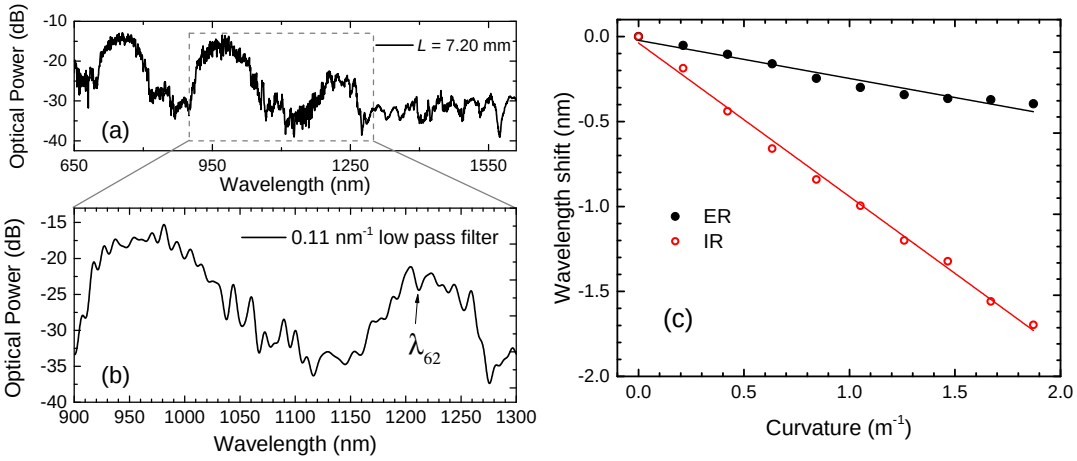

Figure 4.7: (a) Transmission spectrum of the 7.20 mm long sensor, and (b) the respective curve attained by applying a 0.11 nm^{-1} low pass filter on the spectral range of interest. The ER wavelength (λ_{62}) analyzed is also indicated. (c) Wavelength shift dependence with curvature of the ER and IR components.

a linear tendency, leading to curvature sensitivities of $(-0.22 \pm 0.02)\,nm/m^{-1}$ ($r^2 = 0.95064$) and $(-0.90 \pm 0.02)\,nm/m^{-1}$ ($r^2 = 0.99575$), for the ER and IR, respectively. Due to the outer location of the ER, the photoelastic effect is more accentuated. However, the variation in the incident angle of light within the fiber will have a higher impact on the response for smaller structures, namely the silica strands [71]. The dominance of this effect may explain the higher sensitivity of the IR over the ER.

4.2.2 Response to temperature

In the temperature measurements, given that the IR band is considerable large, the monitoring of this component could only be acomplished using a higher temperature range. Therefore, a similar apparatus as figure 4.1 was used, though, a custom designed tubular furnace and a supercontinuum light source were used. The furnace temperature was controlled by a thermocouple with a resolution of 1 °C. The sensor was heated from 50 °C up to 500 °C, in steps of 50 °C. The obtained results, presented in figure 4.8, show a wavelength shift of the ER and IR toward longer wavelengths (red shift). Also, linear responses were attained for both components, achieving temperature sensitivities of $(21.7 \pm 0.3)\,pm/°C$ ($r^2 = 0.99809$) and $(16.6 \pm 0.7)\,pm/°C$ ($r^2 = 0.98517$) for the ER and IR, respectively. According to equation 4.2, temperature sensitivities of $\sim 20.4\,pm/°C$ and $\sim 18.7\,pm/°C$ were expected for both ER and IR. Note that the IR mean wavelength of the loss band is centered near the 1100 nm and the ER dip is close to the 1200 nm. This wide range of wavelengths requires to consider the Sellmeier condition, which provides the refractive index of silica regarding the operating wavelength. Therefore, for the expected sensitivities, it was considered that for the IR $n_{Si} = 1.449$, and the ER $n_{Si} = 1.448$.

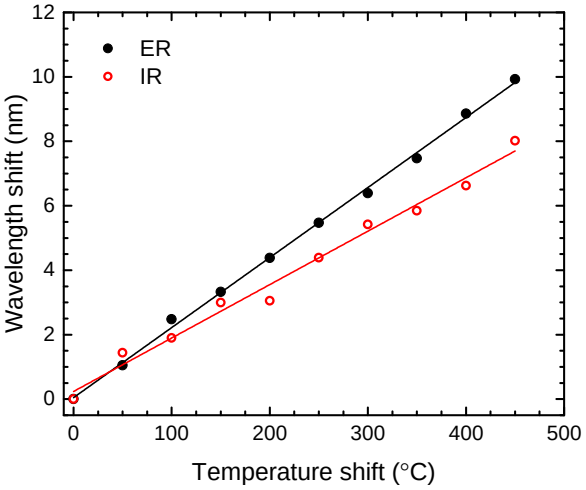

Figure 4.8: Wavelength shift dependence with temperature of the ER and IR components.

4.2.3 Simultaneous measurements of curvature and temperature

The results presented revealed that the sensor resonances had different responses to both curvature and temperature measurements. The ER response ($\Delta\lambda_{\mathrm{ER}}$) and IR response ($\Delta\lambda_{\mathrm{IR}}$), to variations on the curvature (ΔC) and temperature (ΔT) can be described by the following expressions:

$$\Delta\lambda_{\mathrm{ER}} = K_{C,\mathrm{ER}} \cdot \Delta C + K_{T,\mathrm{ER}} \cdot \Delta T, \tag{4.12}$$

$$\Delta\lambda_{\mathrm{IR}} = K_{C,\mathrm{IR}} \cdot \Delta C + K_{T,\mathrm{IR}} \cdot \Delta T, \tag{4.13}$$

with $K_{C,\mathrm{ER}}$, $K_{T,\mathrm{ER}}$ the ER sensitivities to curvature and temperature, respectively, and $K_{C,\mathrm{IR}}$, $K_{T,\mathrm{IR}}$ the respective IR sensitivities to curvature and temperature. Applying the definition of the matrix inversion to the equations 4.12 and 4.13, one attains:

$$\begin{pmatrix} \Delta C \\ \Delta T \end{pmatrix} = \frac{1}{15.9 \times 10^{-3}} \begin{pmatrix} 0.0166 & -0.0217 \\ 0.9 & -0.22 \end{pmatrix} \begin{pmatrix} \Delta\lambda_{\mathrm{ER}} \\ \Delta\lambda_{\mathrm{IR}} \end{pmatrix}. \tag{4.14}$$

Note that the units of ΔC, ΔT, and $\Delta\lambda_{\mathrm{ER,IR}}$ are m^{-1}, °C, and nm, respectively. This outcome potentially enhances the use of this sensor in the simultaneous measurement of these parameters. Without needing a complex design configuration or using several sensing heads but instead, merely resorting to the ARROW guidance properties, makes it a good candidate to wield in several applications.

5. Conclusions and future work

In this work, a novel HSCF was successfully implemented as an OFS. The simple transmission configuration in which the sensor was designed, allied with inner structure of the HSCF, stimulated the occurence of a MMI and a MZI along with the AR guidance. Several studies were implemented and each component of the sensor was thoroughly analysed.

First, a simulation of the ARs in the HSCF was carried out. For the IR, the monitoring of the HE_{11} mode was performed, revealing an asymptotic refractive index behaviour. It was concluded that the asymptotic wavelengths were located in IR frequencies, and were in good agreement with the theoretical IR wavelengths. Furthermore, the effect of IR and ER in the transmission spectrum profile was also analyzed. The modulation of the expected spectrum revealed similar to what was experimentally observed, though the IR wavelengths showed as loss bands, instead of well-defined dips, being this justified by the irregularities on the strands dimensions. In an overall view, the simulation analysis executed to predict the resonances behavior revealed coherent both with the experimental results and with the theoretical model.

A primarily research was conducted to verify the 7.50 mm long sensor response to variations in the refractive index of the external medium, being used glucose aqueous solutions to that end. Both the MMI and the MZI were monitored, being, posteriorly concluded that only the MMI is sensitive to the refractive index, whereas the MZI revealed to be insensitive towards this parameter. Due to the refractive index dependence with the operating wavelength, a calibration on the refractive indices of the glucose solutions was performed. The calibration allowed to achieve a general equation that relates the refractive index of glucose solutions with their mass fractions for a wavelength centered at 1550 nm, being this relation used for the entire experiment. The MMI response with the glucose solutions revealed a nonlinear behaviour with the refractive index, being needed to divide the response into two linear regions. The highest sensitivity was attained for the region between 1.348 RIU and 1.381 RIU with a value of (878 ± 60) nm/RIU. A later study to determine the dependence of the refractive index sensitivity with the HSCF length revealed that there is an optimum length where the sensitivity is maximum for both regions, being near the 11 mm. However, further experiments should be conducted to corroborate this, and to find with more accuracy the optimum length. The sensor resolution was also estimated, achieving a value of 1.09×10^{-4} RIU. Furthermore, a temperature independent refractive index detection was proposed and the TOC of the solutions were also estimated.

In a different experiment, ethanol-water solutions were used with the purpose of monitoring their evaporation profile. The MMI response presented different profiles according to the variation on the ethanol concentration on the solution. It was concluded that water samples evaporate with no change in its refractive index, while solutions that had a percentage of

ethanol presented an initial decrease in the refractive index, due to the ethanol evaporation, followed by a stabilization. For a pure ethanol solution, it was observed an initial increase of the refractive index caused by the hygroscopic properties of the ethanol. These evaporation profiles were observed for both the substrates used, though the experiment may have been influenced by external parameters such as the variation of room temperature and the different strain inadvertently applied to the sensor, causing some dissimilarities in the behaviour of both glass and teflon substrates. It was also observed that, due to the substrate different properties, in the teflon the evaporation process was longer than in the glass. Posteriorly, the spectral responses were successfully converted into a real time variation of ethanol concentration, revealing this promising in future VOCs detection.

Finally, physical parameters were studied in the HSCF sensor. In the experiments carried out in the C+L region, the MMI, MZI and ER responses were monitored towards variations of temperature, bending and strain. For the temperature, sensitivities of $(32.8 \pm 0.4)\,\mathrm{pm/°C}$, $(19 \pm 1)\,\mathrm{pm/°C}$, and $(15.7 \pm 0.5)\,\mathrm{pm/°C}$ were respectively attained for the MZI, ER, and MMI, being in good agreement with the expected values. For the curvature characterization, nonlinear responses were observed, leading to a separation of two curvature regions. For the first region, a highest sensitivity of $(-2.21 \pm 0.08)\,\mathrm{nm/m^{-1}}$ was attained for the MMI, while for the second region a sensitivity of $(-0.63 \pm 0.02)\,\mathrm{nm/m^{-1}}$ was reached by the ER. For the strain characterization, sensitivities of $(0.45 \pm 0.01)\,\mathrm{pm/\mu\varepsilon}$, $(-0.93 \pm 0.04)\,\mathrm{pm/\mu\varepsilon}$, and $(-2.72 \pm 0.09)\,\mathrm{pm/\mu\varepsilon}$ for the MZI, ER, and MMI, were respectively acquired. In the second broadband (900 nm-1300 nm) it was possible to monitor both IR and ER towards variations of temperature and curvature. Curvature sensitivities of $(-0.22 \pm 0.02)\,\mathrm{nm/m^{-1}}$ and $(-0.90 \pm 0.02)\,\mathrm{nm/m^{-1}}$ were obtained for the ER and IR, where the high sensitivity of the IR was explained by the dominance of variations on the incident angle in the silica strands. For the temperature, sensitivities of $(21.7 \pm 0.3)\,\mathrm{pm/°C}$ and $(16.6 \pm 0.7)\,\mathrm{pm/°C}$ were respectively achieved for the ER and IR, being proximate to the expected values.

For future work, a thorough investigation on the HSCF optimum length to achieve a higher sensitivity to refractive index variations is proposed. Furthermore, a complement on the evaporation work should be performed. For example, extend the detection of the ethanol by comparing the method implemented in this work with the conventional imaging process that is typically used. It is also recommended to use the MZI temperature sensitivity to make a temperature compensation, and with this, eliminate possible external influences on the measurement of the evaporation. Still in the evaporation process, it is intended to not only monitor other VOCs, but also to analyze ternary mixtures. Furthermore, it is proposed to further extend the study of the physical parameters by analysing, for instance, the torsion and the lateral force of the sensor to extend the information already retrieved and make this sensor more adequate in a use of a wield of applications. At last, it is also intended to explore this sensor in a different configuration than the transmission layout used in this work, that is, in a reflection configuration, where new interferometers may also appear.

Bibliography

[1] J. Hecht, *City of light : the story of fiber optics*, 1st ed. New York, USA: Oxford University Press, 1999.

[2] R. Tricker, "The history of fiber optics," in *Optoelectronic and fiber optic technology*, 1st ed. Jordan Hill, Oxford, United Kingdom: Newnes, 2002, ch. 1, pp. 1–18.

[3] A. Méndez and T. Morse, "Hollow-core fibers," in *Specialty optical fibers handbook*, 1st ed. San Diego, California, USA: Academic Press, ch. 10, pp. 315–357.

[4] J. M. Senior, *Optical fiber communication: principles and practice*, 3rd ed. Harlow, Essex, England: Pearson Prentice Hall, 2009.

[5] S. Kumar and M. Deen, "Optical fiber transmission," in *Fiber optic communications fundamentals and applications*. Chichester, West Sussex, United Kingdom: Wiley, 2014, ch. 2, pp. 35–91.

[6] E. Udd, "Overview of fiber optic sensors," in *Fiber optic sensors*, 2nd ed., S. Yin, P. Ruffin, and F. Yu, Eds. Boca Raton, Florida, USA: CRC Press, 2008, ch. 1.

[7] J. Joannopoulos, S. Johnson *et al.*, *Photonic crystals molding the flow of light*, 2nd ed. Princeton, New Jersey, United Kingdom: Princeton University Press, 2008.

[8] J. Broeng and D. Mogilevstev, "Photonic crystal fibers : a new class of optical waveguides," *Opt. Fiber Technol.*, vol. 5, pp. 305–330, 1999.

[9] P. S. J. Russell, "Photonic-crystal fibers," *J. Lightwave Technol.*, vol. 24, no. 12, pp. 4729–4749, 2006.

[10] F. Poli, A. Cucinotta, and S. Selleri, *Photonic crystal fibers properties and applications*, R. Hull, R. Osgood *et al.*, Eds. Dordrecht, Netherlands: Springer, 2007.

[11] J. Santos and F. Farahi, *Handbook of optical sensors*. Boca Raton, Florida, USA: CRC Press, 2015.

[12] J. K. Sahota, N. Gupta, and D. Dhawan, "Fiber Bragg grating sensors for monitoring of physical parameters: a comprehensive review," *Opt. Eng.*, vol. 59, no. 6, 2020.

[13] M. De, T. K. Gangopadhyay, and V. K. Singh, "Prospects of photonic crystal fiber as physical sensor: an overview," *Sensors*, vol. 19, no. 3, pp. 1–27, 2019.

[14] S. Rota-Rodrigo, M. López-Amo *et al.*, "Multimodal interferometer based on a suspended core fiber for simultaneous measurement of physical parameters," *J. Lightwave Technol.*, vol. 33, no. 12, pp. 2468–2473, 2015.

[15] J. Shi, G. Su *et al.*, "A dual-parameter sensor using a long period grating concatenated with polarization maintaining fiber in Sagnac loop," *IEEE Sens. J.*, vol. 16, no. 11, pp. 4326 – 4330, 2016.

[16] S. Wang, W. Zhang *et al.*, "Two-dimensional microbend sensor based on long-period fiber gratings in an isosceles triangle arrangement three-core fiber," *Opt. Lett.*, vol. 42, no. 23, pp. 4938–4941, 2017.

[17] T. Zhao, S. Lou *et al.*, "Simultaneous measurement of curvature, strain and temperature using a twin-core photonic crystal fiber-based sensor," *Sensors*, vol. 18, no. 7, pp. 1–11, 2018.

[18] H. Yu, Y. Wang *et al.*, "Fabry-Perot interferometric high-temperature sensing up to 1200 °C based on a silica glass photonic crystal fiber," *Sensors*, vol. 18, no. 1, 2018.

[19] P. Wang, K. Ni *et al.*, "Methylcellulose coated humidity sensor based on Michelson interferometer with thin-core fiber," *Sens. Actuators A Phys.*, vol. 288, pp. 75–78, 2019.

[20] Y. Liu, X. Song *et al.*, "Simultaneous measurement of temperature and strain based on SCF-based MZI cascaded with FBG," *Appl. Opt.*, vol. 59, no. 30, pp. 9476–9481, 2020.

[21] Y. Wang, Y. Zhou *et al.*, "Sensitive Mach–Zehnder interferometric sensor based on a grapefruit microstructured fiber by lateral offset splicing," *Opt. Express*, vol. 28, no. 18, pp. 26 564–26 571, 2020.

[22] B. Pang, G. Zhengtian *et al.*, "Simultaneous measurement of temperature and surrounding refractive index by superimposed coated long period fiber grating and fiber Bragg grating sensor based on mode barrier region," *Optik*, vol. 220, 2020.

[23] K. Nazeri, F. Ahmed *et al.*, "Hollow-core photonic crystal fiber Mach–Zehnder interferometer for gas sensing †," *Sensors*, vol. 20, no. 10, 2020.
[24] A. M. Shrivastav, D. Gunawardena *et al.*, "Microstructured optical fiber based Fabry – Pérot interferometer as a humidity sensor utilizing chitosan polymeric matrix for breath monitoring," *Sci. Rep.*, vol. 10, 2020.
[25] M. Tian, Y. Huang *et al.*, "High-performance humidity sensor based on a micro-nano fiber Bragg grating coated with graphene oxide," *Opt. Express*, vol. 28, no. 18, 2020.
[26] S. Novais, C. I. A. Ferreira *et al.*, "Optical fiber tip sensor for the measurement of glucose aqueous solutions," *IEEE Photonics J.*, vol. 10, no. 5, 2018.
[27] L. Alwis, T. Sun, and K. Grattan, "Developments in optical fibre sensors for industrial applications," *Opt. Laser Technol.*, vol. 78, pp. 62–66, 2015.
[28] C. P. Mayoral, J. G. Gutiérrez *et al.*, "Fiber optic sensors for vital signs monitoring. A review of its practicality in the hyealth field," *Biosensors*, vol. 11, no. 2, pp. 1–32, 2021.
[29] H. Stawska, A. Kolyadin *et al.*, "Hollow-core antiresonant fibers - exploring and enhancing the potential in biochemical detection applications," in *2020 22nd International Conference on Transparent Optical Networks (ICTON)*. Bari, Italy: Proceedings of IEEE 20015282, 2020.
[30] D. Lopez-Torres, C. Elosua, and F. J. Arregui, "Optical fiber sensors based on microstructured optical fibers to detect gases and volatile organic compounds—A review," *Sensors*, vol. 20, no. 9, pp. 1–31, 2020.
[31] E. Cesar, I. R. Matias, and F. J. Arregui, "Volatile organic compound optical fibre sensors: a review," *Sensors*, vol. 6, no. 11, 2006.
[32] M. Yasin, S. W. Harun, and H. Arof, "Optical fiber sensing applications: detection and identification of gases and volatile organic compounds," in *Fiber optic sensors*, M. Yasin, Ed. InTech, 2012, ch. 2, pp. 27–53.
[33] A. Cerqueira, "Recent progress and novel applications of photonic crystal fibers," *Rep. Prog. Phys.*, vol. 73, 2010.
[34] P. S. J. Russell, "Photonic crystal fibers: basics and applications," in *Optical fiber telecommunications VA*, 5th ed. San Diego, California, USA: Academic Press, 2008, ch. 14, pp. 485–522.
[35] K. Schuster, S. Unger *et al.*, "Material and technology trends in fiber optics," *Adv. Opt. Technol.*, vol. 3, no. 4, pp. 447–468, 2014.
[36] J. C. Knight, T. A. Birks *et al.*, "Properties of photonic crystal fiber and the effective index model," *J. Opt. Soc. Am. A*, vol. 15, no. 3, pp. 748–752, 1998.
[37] A. Bjarklev, J. Broeng, and A. S. Bjarklev, *Photonic crystal fibres*, 1st ed. Dordrecht, Netherlands: Springer, 2003.
[38] T. A. Birks, P. J. Roberts *et al.*, "Full 2-D photonic bandgaps in silica/air structures," *Electron. Lett.*, vol. 31, no. 22, pp. 1941–1943, 1995.
[39] F. Couny, F. Benabid *et al.*, "Generation and photonic guidance of multi-octave optical-frequency Combs," *Science*, vol. 318, 2007.
[40] R. Yu, Y. Chen *et al.*, "Hollow-core photonic crystal fiber gas sensing," *Sensors*, vol. 20, no. 10, pp. 1–26, 2020.
[41] A. Argyros, S. G. Leon-saval *et al.*, "Antiresonant reflection and inhibited coupling in hollow-core square lattice optical fibres," *Opt. Express*, vol. 16, no. 8, pp. 5642–5648, 2008.
[42] B. Debord, F. Amrani *et al.*, "Hollow-core fiber technology: the rising of "gas photonics"," *Fibers*, vol. 7, no. 2, 2019.
[43] C. Wei, J. Weiblen *et al.*, "Negative curvature fibers," *Adv. Opt. Photonics*, vol. 9, no. 3, pp. 504–561, 2017.
[44] M. A. Mollah, S. Rana, and H. Subbaraman, "Polarization filter realization using low-loss hollow-core anti-resonant fiber in THz regime," *Results Phys.*, vol. 17, 2020.
[45] A. Iyer, W. Xu *et al.*, "Ultra-low Brillouin scattering in anti-resonant hollow-core fibers," *APL Photonics*, vol. 5, no. 9, 2020.
[46] G. Agrawal, "Introduction," in *Nonlinear fiber optics*, 3rd ed. San Diego, California, USA: Academic Press, 2001, ch. 1, pp. 3–13.
[47] P. A. Agbemabiese and E. K. Akowuah, "Numerical analysis of photonic crystal fiber of ultra - high birefringence and high nonlinearity," *Sci. Rep.*, 2020.
[48] F. Zolla, G. Renversez *et al.*, *Foundations of photonic crystal fibres*. London, United Kingdom: Imperial College Press, 2005.

[49] N. M. Litchinitser, S. C. Dunn *et al.*, "Resonances in microstructured optical waveguides," *Opt. Express*, vol. 11, no. 10, pp. 1243–1251, 2003.
[50] S. Liu, Y. Ji *et al.*, "Humidity-insensitive temperature sensor based on a quartz capillary anti-resonant reflection optical waveguide," *Opt. Express*, vol. 25, no. 16, pp. 18 929–18 939, 2017.
[51] A. Hartung, J. Kobelke *et al.*, "Double antiresonant hollow core fiber – guidance in the deep ultraviolet by modified tunneling leaky modes," *Opt. Express*, vol. 22, no. 16, pp. 19 131–19 140, 2014.
[52] M. Zeisberger and M. A. Schmidt, "Analytic model for the complex effective index of the leaky modes of tube-type anti-resonant hollow core fibers," *Sci. Rep.*, vol. 7, no. 11761, pp. 1–13, 2017.
[53] V. Finazzi, T. M. Monro, and D. J. Richardson, "Small-core silica holey fibers : nonlinearity and confinement loss trade-offs," *J. Opt. Soc. Am. B*, vol. 20, no. 7, pp. 1427–1436, 2003.
[54] W. Sun, X. Zhang *et al.*, "Comparative study on transmission mechanisms in a SMF-capillary-SMF structure," *J. Lightwave Technol.*, vol. 38, no. 15, pp. 4075 – 4085, 2020.
[55] C. Elosua, F. J. Arregui *et al.*, "Micro and nanostructured materials for the development of optical fibre sensors," *Sensors*, vol. 17, no. 10, 2017.
[56] D. R. Lide, *CRC handbook of chemistry and physics*, 86th ed. Boca Raton, Florida, USA: CRC Press, 2005.
[57] J. E. Saunders, C. Sanders *et al.*, "Refractive indices of common solvents and solutions at 1550 nm," *Appl. Opt.*, vol. 55, no. 4, 2016.
[58] Y. Zhao, L. Cai *et al.*, "Investigation of the high sensitivity RI sensor based on SMS fiber structure," *Sens. Actuators A Phys.*, vol. 205, 2014.
[59] Y. Cardona-maya, I. D. Villar *et al.*, "Wavelength and phase detection based SMS fiber sensors optimized with etching and nanodeposition," *J. Lightwave Technol.*, vol. 35, no. 17, 2017.
[60] R. Romero, O. Frazão *et al.*, "Intensity-referenced and temperature-independent curvature-sensing concept based on chirped fiber Bragg gratings," *Appl. Opt.*, vol. 44, no. 18, pp. 3821–3826, 2005.
[61] V. I. Ruiz-perez, P. M. Velasco-Bolom *et al.*, "Measuring the thermo-optic coefficient of liquids with athermal multimode interference devices," *IEEE Sens. J.*, vol. 21, no. 3, 2021.
[62] S. Novais, M. S. Ferreira, and J. L. Pinto, "Determination of thermo-optic coefficient of ethanol-water mixtures with optical fiber tip sensor," *Opt. Fiber Technol.*, vol. 45, pp. 276–279, 2018.
[63] C. Elosua, C. Bariain, and I. R. Matias, "Optical fiber fensing applications: detection and identification of gases and volatile organic compounds," in *Fiber optic sensors*, 1st ed., M. Yasin, S. W. Harun, and H. Arof, Eds. InTech, 2012, ch. 2, pp. 27–52.
[64] K. Sefiane, L. Tadrist, and M. Douglas, "Experimental study of evaporating water – ethanol mixture sessile drop : influence of concentration," *Int. J. Heat Mass Transf.*, vol. 46, no. 23, pp. 4527–4534, 2003.
[65] D. Brutin and V. Starov, "Recent advances in droplet wetting and evaporation," *Chem. Soc. Rev.*, vol. 47, no. 2, pp. 558–585, 2018.
[66] L. Middelburg, G. de Graaf *et al.*, "Multi-domain spectroscopy for composition measurement of water-containing bio-ethanol fuel," *Fuel Process. Technol.*, vol. 167, pp. 127–135, 2017.
[67] R. Gao, D. Lu *et al.*, "Self-referenced antiresonant reflecting guidance mechanism for directional bending sensing with low temperature and strain crosstalk," *Opt. Express*, vol. 25, no. 15, pp. 18 081–18 091, 2017.
[68] Y. J. Rao, "In-fibre Bragg grating sensors," *Meas. Sci. Technol.*, vol. 8, no. 4, pp. 355–375, 1997.
[69] J. F. Shackelford and W. Alexander, *Materials science and engineering handbook*, 3rd ed., J. F. Shackelford and W. Alexander, Eds. Boca Raton, Florida, USA: CRC Press, 2001.
[70] Y. Liu and L. We, "Low-cost high-sensitivity strain and temperature sensing using graded-index multimode fibers," *Appl. Opt.*, vol. 46, no. 13, pp. 2516–2519, 2007.
[71] W. Ni, P. Lu *et al.*, "Single hole twin eccentric core fiber sensor based on anti-resonant effect combined with inline Mach-Zehnder interferometer," *Opt. Express*, vol. 25, no. 11, pp. 12 372–12 380, 2017.